Seismic structure around the 660 in subduction zones and its implications

A Dissertation
SUBMITTED TO THE FACULTY OF
UNIVERSITY OF MINNESOTA
BY

Tao Wang

IN PARTIAL FULFILLMENT OF THE REQUIREMENTS
FOR THE DEGREE OF
DOCTOR OF PHILOSOPHY

Justin Revenaugh

June, 2013

Acknowledgements

I firstly wish to express my sincere thanks to my advisor, Justin Revenaugh, who painstakingly supervised and directed my activities throughout the programme. Without Justin's advice, revision and hard work, this thesis would not have been written. Last five years, his broad knowledge and insightful thoughts inspired me to complete this research.

Besides my advisor, my immense gratitude goes to my committee members, Professor David Kohlstedt, Marc Hirschmann and Martin Saar. They provided valuable comments to this research. I appreciate Department staff Sharon Kressler, Kathy Ohler, Doug Johnson, Greg Gambeski and so on. Their tremendous assistance offered great convenience to my American life.

I acknowledge the staff working in Minnesota Supercomputing Institute. They offered great assistance for me to run parallel computing program.

I thank my friend Dr. Ling Chen for enlightening me the first glance of research. Also I thank my labmates Brian Bagley and Xiaoyue Ma for the time we were working together.

My wife, Fang Fang and my Parents, Keying Liu and Xiangqi Wang were exceedingly supportive. To them I owe a huge bundle of gratitude for understanding my work. In particular, after the birth of my son, Kunyu Wang in Feb 2012, they spent lots of time to take care of him so I could focus on this research.

Dedication

This work is dedicated to Fang Fang (my dear wife), Kunyu Wang (my lovely son) and my parents (Xiangqi Wang and Keying Liu).

Abstract

Velocity structure around the 660-km seismic discontinuity in subduction zones is crucial for understanding the thermal state, chemical composition, and dynamics of the mantle. Because of limited spatial coverage of data and resolution, the complicated structure, especially in sub-slab regions, remains ambiguous.

Topographic variation of the oceanward 660-km discontinuity in the Western Pacific is investigated by stacking S-to-P converted phases using large-array data. Beneath the Philippine Sea and Southern Kuril Islands, the mean depth of this discontinuity is elevated ~10 km and ~6.5 km with respect to the global average depth. Meanwhile, it is normal beneath the Sea of Japan where the subducted slab appears to be near-horizontally flattened above the 660-km discontinuity. Elsewhere, the 660-km discontinuity is ~11.5 km and ~6.4 km shallower beneath the Marianas and Tonga Islands subduction zones, respectively. This topographic variation suggests that the 660-km discontinuity beneath subducting slabs shallows as the dip of the slab increases.

Using sources in the western Pacific and stations in China, 3D triplication waveform modeling of structure beneath the Southern Kuril subduction zone suggests that the high-velocity slab (+5% anomaly and ~100km thick) subducts to at least 560 km. No obvious high-velocity anomaly of the slab is observed around the 660 km depth. To match late AB and BC branch arrives at large distances, one of two possible low-velocity anomalies (-3% and ~30km thick) is necessary. The first is located beneath the subducted slab and might be due to a hot sinking anomaly emplaced at shallower depths away from the subduction zone. The second location is on the landward side of the subducted slab

and above the 660-km discontinuity. We suggest this low-velocity anomaly could be generated by hot upwelling from lower mantle or small scale convection above the deep slab.

Numerical modeling of mantle convection demonstrates that slab entrainment of hot sinking anomalies can explain both the topographic variation of the 660-km discontinuity oceanward of slabs and the possible low-velocity anomaly beneath the subducted slab in the Southern Kuriles.

Table of Contents

List of Tables

List of Figures

Chapter 1, Introduction

1.1 Subduction zone

Subduction plays a major role in dynamics of the mantle convection and the movement of water in the planet. Because most mantle rock samples come from depths less than 200 km, geophysical observations, especially seismic structure in subduction zones, are fundamental to understanding the thermal state, chemical composition and dynamics of the mantle. The combination of strong thermal and chemical anomalies coupled with multiple significant mineral phase transitions and disassociations produce some of the most complex imaging problems in seismology.

Subduction zone regassing is the most important process of returning water to Earth's mantle. Most of the water is carried to depth in hydrous minerals. Serpentine is indicated to be a possible water carrier into the 150- to 200-km depth range [*Kawakatsu and Watada*, 2007] and lawsonite (stable above ~400 km) might play a major role on carrying water into the transition zone [*Karato*, 1993; *Williams and Hemley*, 2001]. Tonegawa et al [2008] argue that hydrated oceanic crust would dehydrate during subduction, and that nominally-anhydrous minerals (NAMs) and phase A in the mantle wedge could carry water below the 410 km. In addition, superhydrous B and phase D (Dense Hydrous Silicates) are regarded as possible hosts to bring water downward through the 660-km discontinuity in subducted slabs [*Frost and Fei*, 1998; *Ohtani et al.*, 2004]. The transition zone may be a possible water reservoir because of the high water solubility of wadsleyite and ringwoodite compared to olivine and perovskite. Wadsleyite-olivine partition coefficients are about 5~6 [*Chen et al.*, 2002; *Kohlstedt et al.*, 1996],

which indicates wadsleyite could contain 2~3wt% H2O in the transition zone. Ringwoodite has similar water solubility comparable to wadsleyite [*Inoue et al.*, 1998; *Kohlstedt et al.*, 1996; *Ohtani et al.*, 2000]. While it is clear that water can be stored in significant volumes in the transition zone, the question of whether or not subducted water is brought to those depths (or deeper) is still under debate [*Bercovici and Karato*, 2003; *Hirschmann*, 2006; *Karato*, 2011; *Meier et al.*, 2009; *Van der Meijde et al.*, 2003; *Yoshino et al.*, 2008].

1.2 The 660-km discontinuity

The seismic discontinuity near depth of 660 km (hereafter called the 660) marks a strong change in seismic velocity and was studied intensively in the past several decades [*e.g. Shearer* 1991b]. Conventional wisdom has the 660 arises from the disassociation of ringwoodite to perovskite + magnesiowustite [*Bina and Helffrich*, 1994; *Fei et al.*, 2004; *Ringwood*, 1991]. Due to the negative Clayperon slope, the endothermic disassociation of ringwoodite results in a shallower (deeper) 660-km discontinuity in hot (cold) areas. This offsets thermal buoyancy, presenting an impediment for upwelling hot plumes and subducting cold slabs. Hence, the 660 is often regarded as the boundary between the upper and lower mantles. Tomographic imaging shows strong interactions between subducting slabs and the 660 with some slabs bent to lay flat along the boundary and others penetrating but thickening in the lower mantle [*e.g. Van der hilst et al.*, 1991]. The latter observations demonstrate that, while an impediment to thermal-buoyancy driven flow, the 660 does not mark the boundary between convectively isolated mantles.

There are, however, many unknowns in seismic structure near the 660, especially under subduction zones. This is because seismic structure near the 660-km discontinuity is complicated by phase changes of non-olivine components and by changes in composition. Based on mineral physics calculation and high-pressure experiments, the transformation from garnet to perovskite can produce significant seismic structure near the 660, especially in cold environments [*Vacher et al.*, 1998]. This was used to interpret observations of multiple "660" discontinuities in subduction zones [*Ai et al.*, 2003; *Niu and Kawakatsu*, 1998; *Tibi et al.*, 2007].

Al, Fe and water also influence seismic structure near the 660 [*Inoue et al.*, 1995; *Smyth et al.*, 2004; *Wang et al.*, 2008; *Weidner and Wang*, 1998; *Weidner and Wang*, 2000]. For instance, wet conditions near 660-km depth would depress the disassociation of ringwoodite while uplifting the transition of garnet to perovskite. The difficulty of isolating these various contributions to seismic structure limits what we can learn about temperature and composition near the base of the transition zone.

To provide convincing constraints on thermal state, composition and dynamics around the 660 in subduction zones, seismic structures, including seismic velocity (Vp and/or Vs), depth of the discontinuities and anisotropy, are the most direct and effective tool.

Regional tomography image indicated high velocity anomaly for the cold slab could be up to +5% at 110 km depth [*Zielhuis and Nolet*, 1994]. However, typically, the heterogeneity is ±3% around 100 km depth but less than ±1% in the transition zone [*Gudmundsson and Sambridge*, 1998]. Furthermore, low-velocity structure has been

frequently observed in the mantle wedge above the slab and interpreted as being caused either by hot upwelling flow or by the presence of volatiles, which may directly result from the dehydration reaction in the slab [*Nolet et al.*, 1994; *Revenaugh and Sipkin*, 1994; *Zhao et al.*, 2001]. Recently, several studies revealed low-velocity anomalies beneath subducted slabs [*Obayashi et al.*, 2006; *Wang and Chen*, 2009; *Zhao et al.*, 2007], which might cause by an upwelling plume [*Obayashi et al.*, 2006], a sinking hot anomaly [*Honda et al.*, 2007] or the complex configuration of convergent plate boundaries [*Lowman et al.*, 2007]. It is undoubted that details of seismic anomalies in subduction zones can provide more evidences to test those dynamic models.

The region between the 660 and the discontinuity near 410 km (hereafter called the 410) is usually referred as mantle transition zone. Besides the 660, the 410 and the 520-km discontinuity (hereafter called the 520) in mantle transition zone are caused by the phase transition of olivine to wadsleyite and wadsleyite to ringwoodite, respectively [*Bina and Helffrich*, 1994; *Fei et al.*, 2004; *Ringwood*, 1991]. But the 520 is less commonly observed [*Andrews and Deuss*, 2008; *Gu et al.*, 1998; *Gu and Dziewonski*, 2002; *Revenaugh and Jordan*, 1991]. Before subducting slabs reach the 660, they must penetrate the 410 and the possible 520. Therefore, seismic structure around the 410 and the 520, especially topographic variations, can provide additional information to investigate the 660. For example, for low temperature, the 410 is uplifted but the 660 is depressed because of the opposite Clayperon slope if olivine component is the main factor to vary the topography. In the subduction zone, if their behaviors disobey it, this may indicate other significant factors [*Schmerr and Garnero*, 2007].

Anisotropy is the third means to constrain the fundamental conditions, especially reflecting the dynamics in time domain. Traditionally, anisotropy is thought to be mainly contributed by the upper 300 km in the mantle. However, more and more studies indicate strong anisotropy may exist below 300 km and even in the mantle transition zone [*Di Leo et al.*, 2012; *Foley and Long*, 2011]. This means anisotropy around the 660 may shed light on subduction process. Nevertheless, anisotropy will be investigated in the future research but not in this study.

1.3 Structure beneath subducting slabs

Great progress has been made in imaging structure above subducting slabs where abundant local seismicity and dense regional arrays frequently offer excellent coverage studies [*Kawakatsu and Watada*, 2007; *Nolet et al.*, 1994; *Revenaugh and Sipkin*, 1994; *Tonegawa et al*., 2008; *Zhao et al*., 2001]. Less is known about structure beneath slabs, areas that are more difficult to access seismologically. Although tomography indicates more subdued velocity variability beneath slabs generally, there are reasons to further explore these areas.

1. Low-velocity anomalies beneath the descending high-velocity slabs were observed in a number of subduction zones sampled by regional and global tomographic studies [*Huang and Zhao*, 2006; *Zhao et al.*, 1994; *Zhao et al.*, 2007]. Decreasing resolution with depth and possible trade-off between high and low velocities, however, make it difficult to fully substantiate these features or to evaluate their vertical extent. A sub-slab low velocity zone has been verified by triplication waveform modeling in

several places beneath the northwestern Pacific [*Obayashi et al.*, 2006; *Wang and Chen*, 2009], but whether these slow structural features are the norm or occasional exceptions remains unclear. A hot plume rising up to the subduction zone [*Obayashi et al*., 2006; *Wang and Chen*, 2009] and a sinking hot anomaly dragged down by the subducting slab [*Honda et al*., 2007] have been proposed as possible mechanisms to explain them. Exploration of fine seismic structure under subducting slabs is needed to confirm low-velocity anomalies in tomographic images and investigate possible causes.

2. While recent electrical conductivity studies suggest the mantle transition zone is generally dry (less than 0.1wt% in [*Yoshino et al.*, 2008] and 0.1wt%~0.2wt% in [*Huang et al.*, 2005]), it may trap water because of high hydrogen solubility in wadsleyite and ringwoodite compared with olivine and perovskite [*Bercovici and Karato*, 2003], especially in high-supply regions, i.e., subduction zones. It lowers seismic velocities by increasing anelastic relaxation and decreasing the bond strength of minerals [*Karato*, 1995]. In the transition zone, hydration appears to have a larger effect on S than P velocity, so that the velocity ratio (Vp/Vs) varies strongly with hydration [*Jacobsen et al*., 2004; *Smyth et al*., 2004]. Water also changes the two-phase loop width and depth of discontinuities, and hydrated material moving out of the transition may melt as it undergoes transitions to mineral phases with lower water solubility [*Hirschmann, 2006*; *Revenaugh and Sipkin*, 1994; *Schmerr and Garnero*, 2007; *Zheng et al*., 2007]. All of these calling cards are important in seismic hygrometry. Hydration level beneath subducting slabs is an important comparison point as sub-slab mantle should be isolated from the dehydration processes active in and above the slab.

3. Based on the correlation between anisotropy magnitude and trench migration velocity, trench-parallel anisotropy in the mantle wedge, which is controversial with traditional theory of A-type olivine LPO (Lattice Preferred Orientation), might be caused by the 3D flow around slabs induced by trench migration [*Long and Silver*, 2008]. To test this, we must know, among other things, conditions below the slab where, for instance, low-velocity anomalies have been imaged.

In the second chapter, we use global broadband array data to identify small-amplitude source-side S to P conversions at transition zone discontinuities in late P wave coda. This method opens access to sub-slab transition zone structure in the western Pacific. Stacking arrivals over large arrays increases resolution in theory, but presents problems in practice. To demonstrate that it works, we first compare it against data from dense broadband arrays. We further verify the method by investigating the better known topographic variations of the 410-km and 660-km discontinuities above the slab. We then turn to sub-slab topography of the 660-km discontinuity and its causes.

In chapter 3, we discuss the differences between 1D and 3D simulations for triplication waveform modeling under the subduction zone. In particular, the influence of lateral heterogeneity for 1D method is discussed. Moreover, SH velocity anomaly beneath northeast Asia is unveiled by 3D waveform modeling. In this region, previous 1D triplication waveform modeling showed distinct velocity variations around the base of mantle transition zone, especially low SH velocity anomaly near the 660 [*Wang and Chen*, 2009]. Our 3D waveform modeling reveals two possible lateral positions for the

low velocity anomaly.

In chapter 4, we try to find the possible dynamic mechanisms through numerical modeling. Two models with different dipping angles will be designed and ran to test the hot sinking anomaly mechanism.

Chapter 2, Depth variations of the discontinuities

Many common seismic imaging methods struggle to constrain the structure and fine topography of the 660 beneath subducting slabs. Subduction zone tomography is not strongly sensitive to topographic variation of discontinuities and its resolution around 660 km, especially beneath slabs, is limited. The paucity of ocean-bottom seismographs and their generally noisy horizontal components limits the use of receiver functions to study the 660 beneath subducting slabs. PP or SS precursors are typically used to study long wavelength topography (bin size >1000 km [*Schmerr and Garnero*, 2007]) making it difficult to isolate near-slab structure. The same is true of ScS reverberations which produce path averages that seldom are pure sub-slab. In this chapter, to study the topography of the 660, we use source-side S-to-P converted phases recorded by large arrays in both dip and anti-dip directions.

2.1 Method and data

We examined all available large (magnitude Mb>5.5) and deep (focal depth>100 km) earthquakes from 1990 to 2009 available through IRIS in the region of 30°~55°N, 120°~150°E. We excluded shallower events to avoid interference with high-amplitude pP and sP phases. Only vertical component seismograms, with clear direct P phase and relatively simple source time functions were retained. Traces whose source-side S to P converted phases are possibly overprinted by other phases (e.g. pP, sP and PcP) were deleted. Lastly, recordings outside the distance range of 30° to 90° were discarded to avoid triplicated arrivals and minimize contamination by D" and core phases.

Seismograms were deconvolved to ground displacement in order to remove the effects of disparate instrumentation.

Our targets are the SdP phases originating on the source side. Here SdP refers to a shear-wave exiting the source volume and converting to P at a discontinuity with nominal depth d (see Figure 1). The travel time delay of SdP to P depends on many factors (e.g., source depth, epicentral distance, and P and S wave velocity in the source region) which must be accounted for is we are to meaningfully extract discontinuity depth variation. Figure 1 shows that raypaths of teleseismic events are near perpendicular to the discontinuities in the mantle transition zone and that the raypaths of SdP and P effectively overlap over most of their length and will respond equally to along-path velocity heterogeneity. Pds phases (waves converted from P to S at discontinuities beneath the stations) are differentiated from SdP on the basis of travel time and, if missed, would map to structure at least 100 km deeper than the source-side interpretation (100 km is the minimum earthquake depth) a distance far outside seismic observations of discontinuity topography.

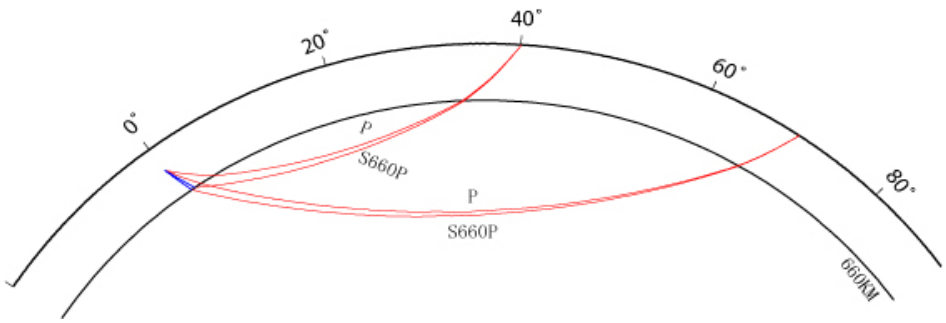

Figure 1: Examples raypaths of P and S660P at distances of 40° and 70°. Blue and red segments represent S and P legs, respectively.

For our experiment, the two most important controls on the precision and accuracy of discontinuity depth estimates are hypocenter mislocation and source-side velocity heterogeneity. The dependence of conversion point depth on travel time difference results in errors in depth estimates equals in magnitude and sign to errors in focal depth (Fig. 2). To minimize these, we relocated all events as discussed later.

To examine the influence of source-side velocity heterogeneity, we define:

Residual = $(t_{SdP}-t_P)_{model}-(t_{SdP}-t_P)_{IASP91}$ for theoretical travel-time calculations

or

Residual = $(t_{SdP}-t_P)_{observation}-(t_{SdP}-t_P)_{IASP91}$ for measured travel times.

Figure 2 shows theoretical travel-time differences between P and SdP for a variety of different 1D models. These models show that source-side velocity variations have only a small influence on depth estimates. For instance, a model with S velocity ~1% lower in the 100 km interval above the 660 but normal P velocity (as compared with IASP91 [*Kennett and Engdahl*, 1991]) produces a residual of ~0.2s (Fig. 2c and 2d) which equates to roughly a 2 km depression of the inferred depth of conversion. If both S and P velocity are reduced by 1% the residuals are much smaller (~0.06s equating to ~0.4 km depth; see Fig. 2e and 2f). Even for ~2% lower S and unchanged Vp, the residuals are only 0.4s (Fig. 2h and 2g). Variations of discontinuity depth, as well as the uncertainty of source depth, could affect the residuals significantly. 20 km depression of the 660-km discontinuity has similar residuals (~2s) as 20 km shallow focal depth (Fig. 2a). It is worth noting, in this context, that residuals vary little with distance from 30° to 90° such

that data stacks in a large distance will not be strongly impacted by small velocity perturbations in the source region.

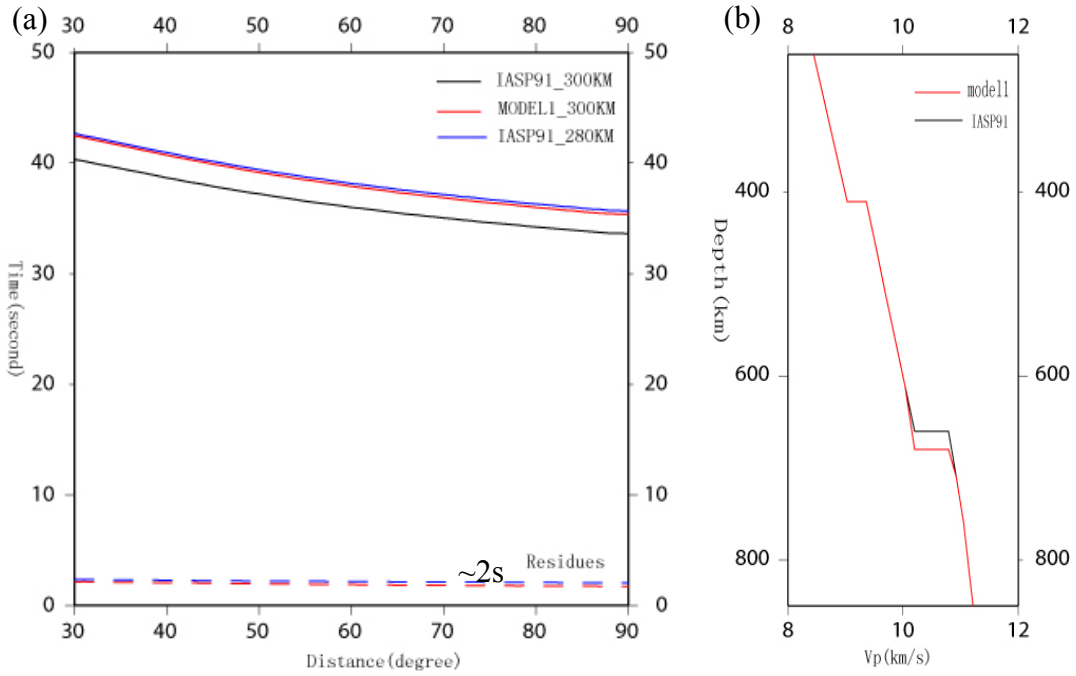

Figure 2: Comparison of travel-time differences (solid lines in a, c, e and g) and residuals (dashed lines in a, c, e and g) between the IASP91 and perturbed models (b, d, f and h). Except IASP91_280KM (blue lines in a) using 280km as focal depth, all calculations are based on the source depth at 300km. Model1 (a and b) moves the 660 to 680 km depth. Model2 (c and d) decreases Vs a net of 1% over 100km above the 660 (linear change from 0% at 560 km to 2% at 660 km) but keeps Vp unchanged. Model3 (e and f) decreases both Vs and Vp equally with Vs as in model2. Model4 has average ~2% lower Vs in lowermost 100km of the transition with no change Vp (g and h).

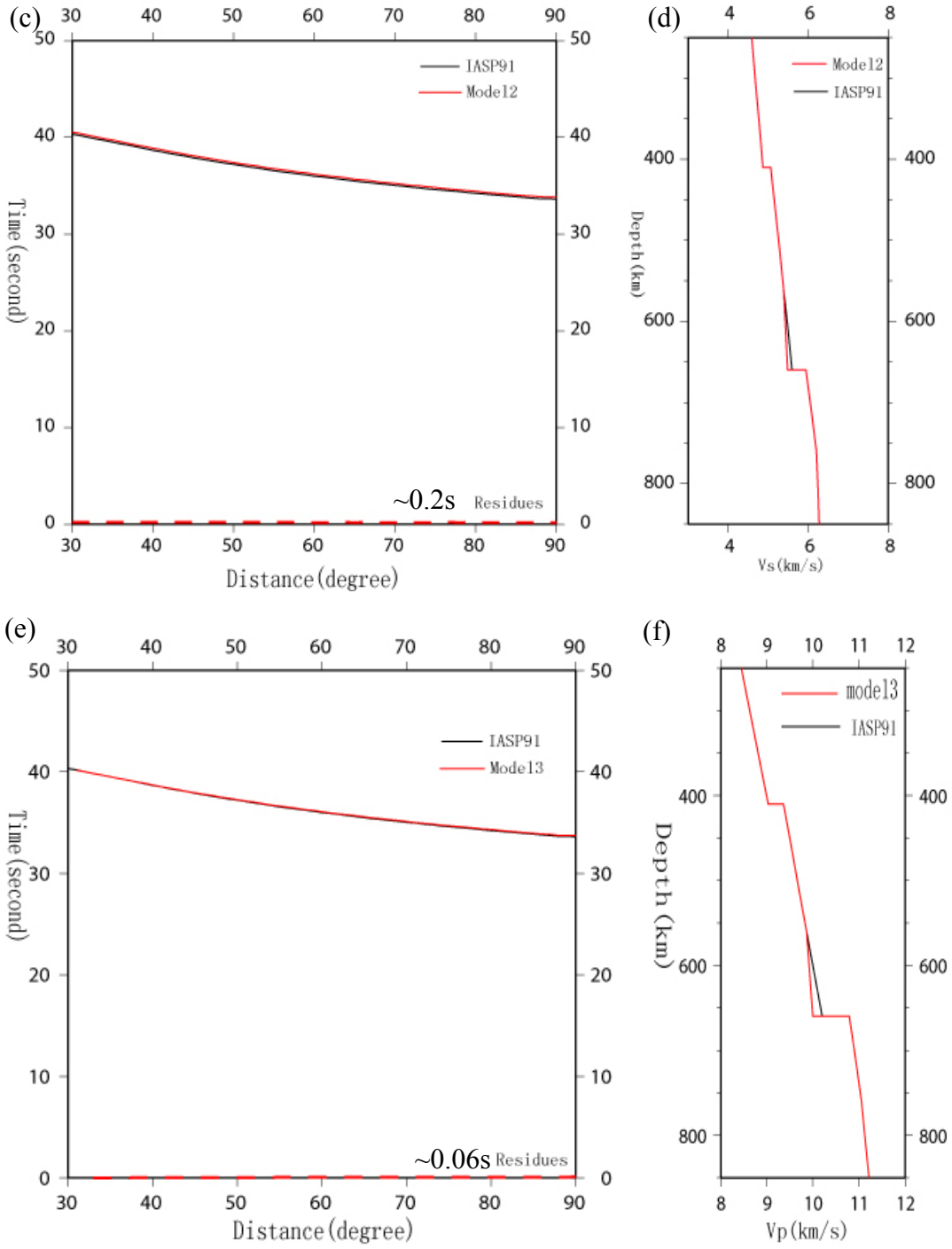

Figure 2 (*continued*)

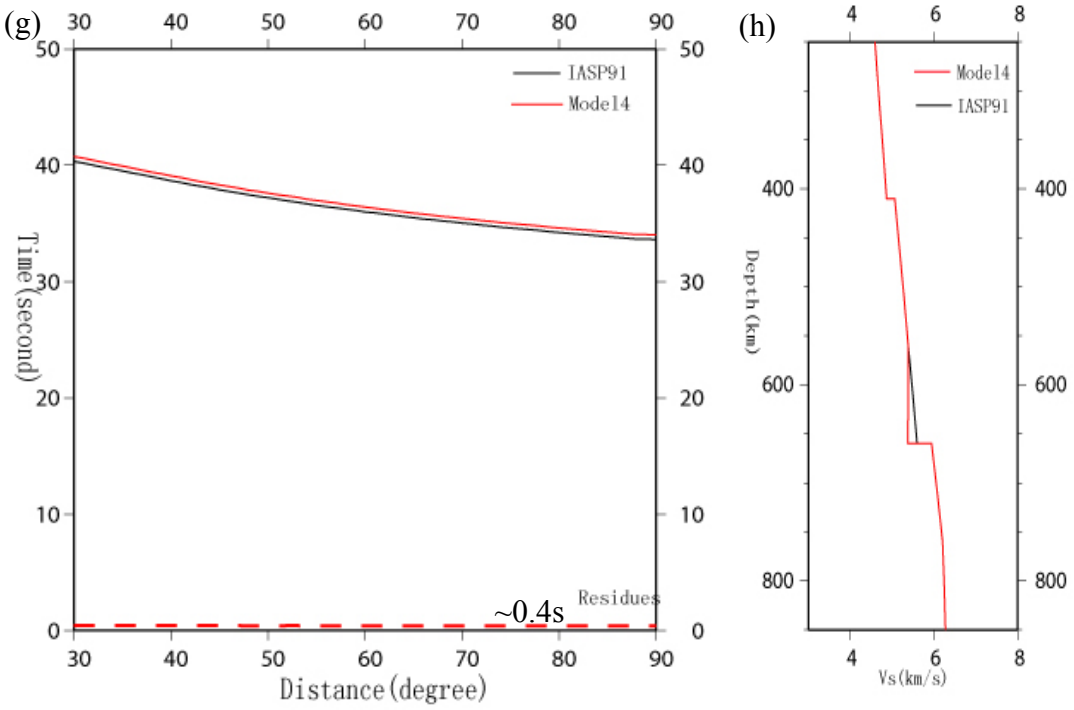

Figure 2 (*continued*)

Next, we consider what might affect the visibility of the converted phases. The amplitude ratio of SdP to P depends primarily on the impedance of discontinuities and focal mechanism. Two deep events with clear direct P were selected to demonstrate the influence of focal mechanism. Because of the simple P waveforms recorded at the distant stations for these deep earthquakes, a normalized square half-sinusoid wavelet was chosen as the input source time function in synthetic calculation. The focal mechanisms used in this study were from the Harvard centroid moment tensor (CMT) solutions (Table 1, Fig. 3a). Synthetics were calculated using the reflectivity method [*Wang*, 1999]. S660P is clearly seen in synthetics and observations for event 2000.07.10 (Fig. 3c and 3e), while it is hard to track S660P in event 2001.02.26 (Fig. 3b and 3d). Because of this strong

dependence on source mechanism, as well as other effects such as attenuation, discontinuity width, etc., we have chosen to focus on travel time and disregard amplitude information.

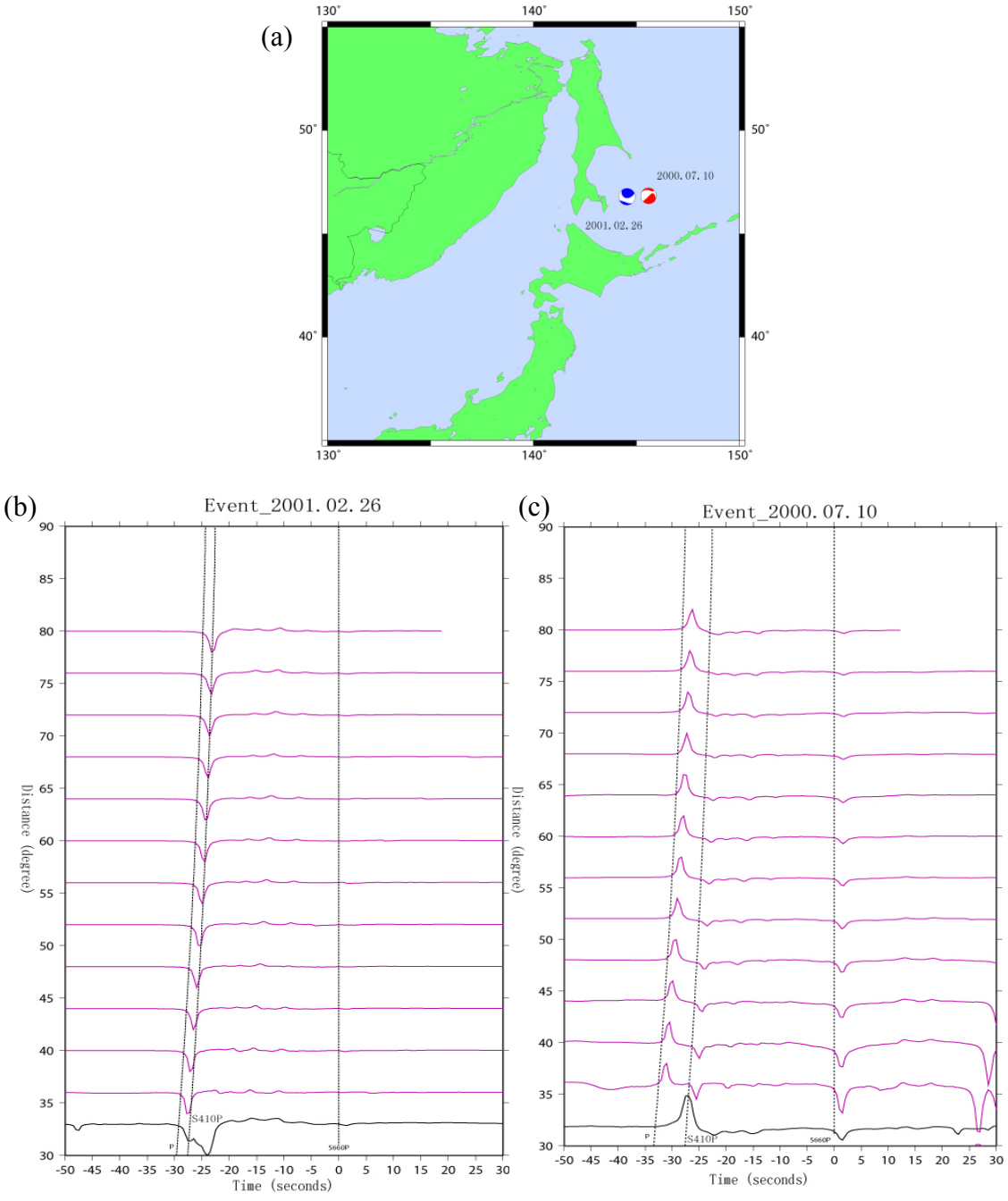

Figure 3 *(to be continued)*

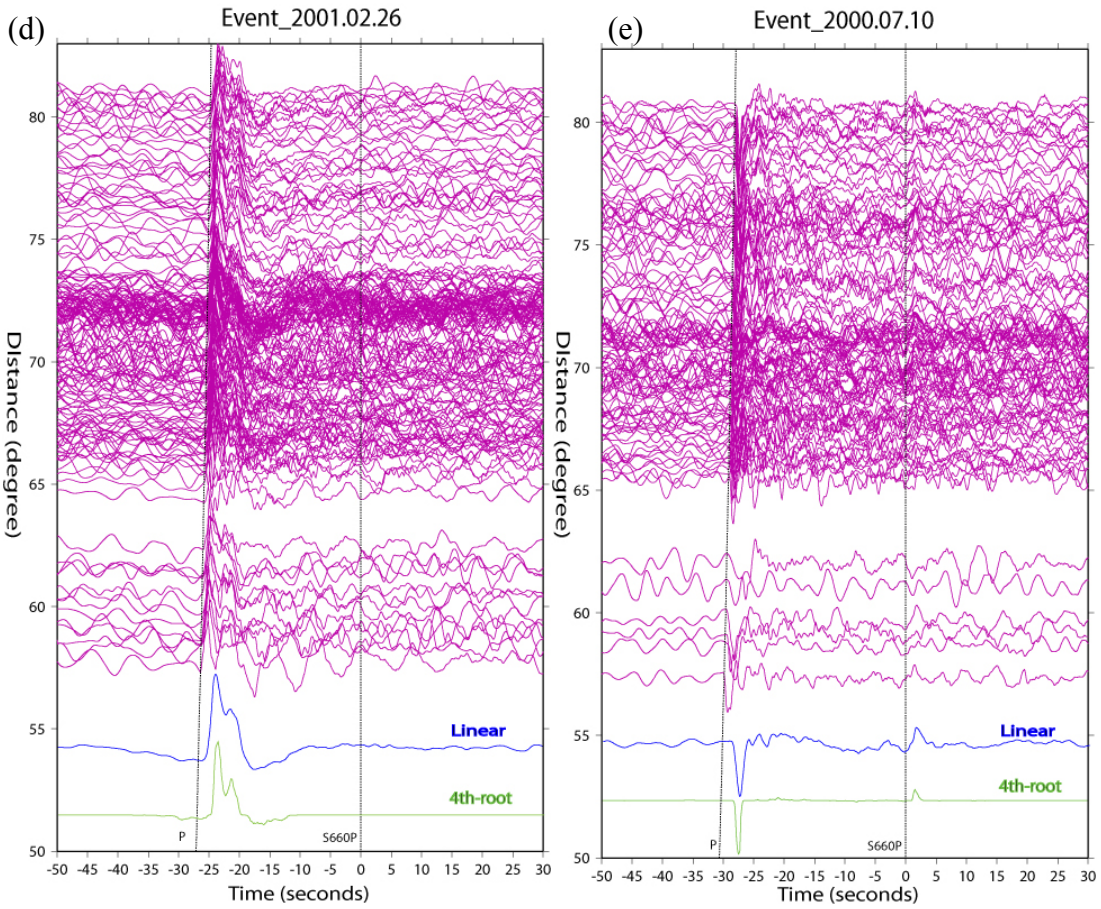

Figure 3: Two events demonstrating the influence of focal mechanism on the amplitude of S660P. Source mechanism data is from Harvard CMT (a). Synthetics (red lines in b and c) and theoretical travel-time (black dash lines in b, c, d and e) are calculated based on IASP91. Observed data is plotted using red lines in d and e. Results of linear (black lines in b and c, blue lines in d and e) and 4th-root (green lines in d and e) stacking are plotted, which are aligned along the phase S660P.

Table 1
Events used for illustrating the influence of focal mechanism and the misleading vespagram

Event	Latitude °N	Longitude °E	Depth (km)	Strike (°)	Dip (°)	Slip (°)
2000.07.10	46.83	145.59	361.3	290	36	-24
2001.02.26	46.79	144.54	396.4	164	52	27
2008.07.23	39.73	141.51	108[(a)]	14	18	-75

Values are all from the Harvard Centroid Moment Tensor (CMT) except the depth [(a)] of event 2008.07.23, which is from FARM catalog in IRIS. Because this depth is more consistent with the depth phase sP (Fig. 4).

Even for an event with a favorably oriented source, it is difficult to robustly identify SdP phases in individual records, mandating use of a stacking method to enhance the low signal-to-noise ratio (SNR) of the converted phases. We applied a multi-step process for enhancing and quantifying SdP. First, all traces were normalized by the amplitude of direct P on an event by event basis. Second, records were 4th root stacked along calculated SdP travel-time trajectories based on IASP91 to identify converted phases and determine their polarity (Fig. 3e). We carefully examined each stack for signs of reverberations or Pds interference, rejecting any stack thought to be affected within the SdP window. 4th root stacking is better at damping incoherent spikes than linear stacking [*Mcfadden et al.*, 1986; *Rost and Thomas*, 2002], but can strongly distort waveforms

resulting in imprecise travel time measurements [*Mcfadden et al.*, 1986]. Thus, in the third step, we employed linear stacking to obtain travel-time residuals. Even with stacking, it is difficult to estimate the onset time of SdP. Instead of the onset time, we picked the maximum amplitude time of SdP in stacked seismograms within a ± 5 s window centered on the theoretical arrival time. The peak was constrained to have the same polarity as was determined by the 4th root stacking in the second step. In the fourth step, the half source time function was calculated by linear stacking of the direct P phase. Finally, we obtained the observed travel-time residuals of phase SdP by removing the source half duration from the travel-time of SdP estimated in the third step.

In outline, we are following previous studies [*Kaneshima and Helffrich*, 1999; *Li et al.*, 2008; *Niu and Kawakatsu*, 1995; *Rost and Thomas*, 2002; *Zang et al.*, 2006] in stacking data on an event by event basis. Where we differ is that most previous studies have stacked data from dense, small-aperture seismic arrays. Use of small arrays results in destructive interference from velocity heterogeneity and waveform variability, but does introduce the possibility of mistaking some other arrival for SdP given limited slowness constraints. For example, using data in a narrow distance range (78°~81°) for event 2008.07.23, both time-distance curves (Fig. 4b) and the vesparagram (Fig. 4c) appear to show S660P. Use of a larger distance window (63°~90°, Fig. 4a) reveals problems with this identification. Relative to direct P, the observered slowness (red dashed line in Fig. 4a) is positive, which contradicts the negative slowness expected for S660P. Given the almost parallel slowness, multiple reflections of direct P are our preferred interpretation of this phase. Benefiting from constant residuals in a large

distance range (Fig. 2), we found that it was feasible to observe converted phases after stacking all available teleseismic (30°~90°) observations. While we are almost certainly missing some SdP phases by stacking over such a large window, we have greater confidence in our identifications in those cases where a clear candidate phase emerges in the stacks.

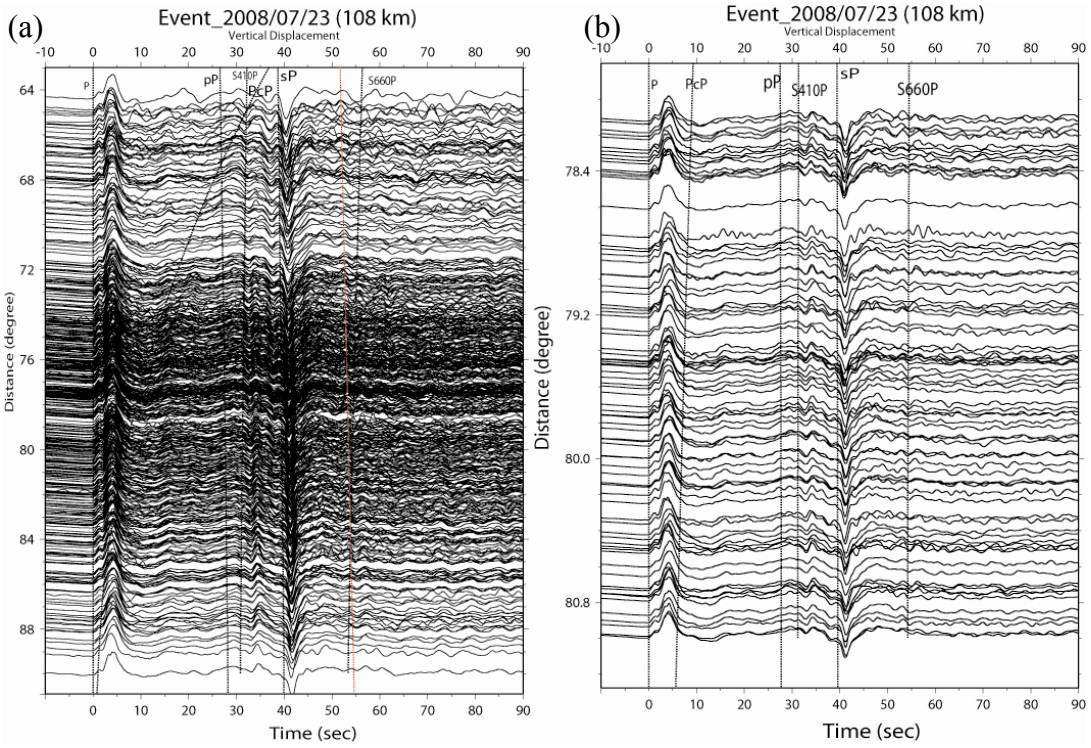

Figure 4 *(to be continued)*

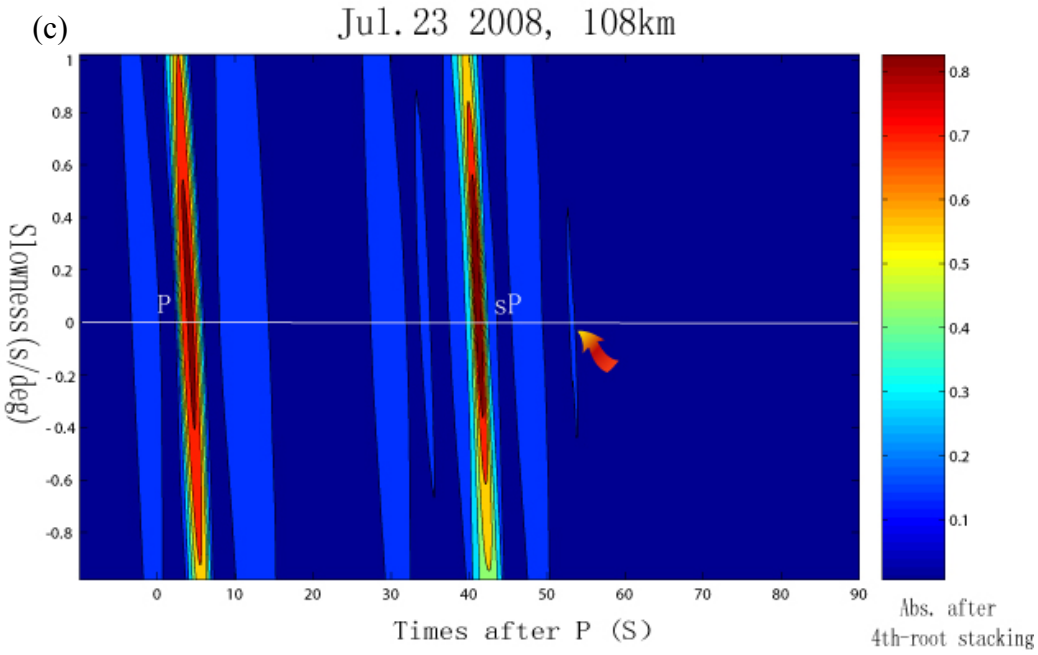

Figure 4: Vespagram analysis withing a narrow distance range demonstrating the difficulty of distinguishing the slowness difference between converted phases and multiple reflections of direct P. Available seismograms in a distance range of 63°~90° are plotted (a); black dashed lines are theoretical travel-time based on IASP91 (a, b). The red dashed line (a) is the observed slowness (positive) and obviously deviates from calculated slowness of phase S660P. However, in a small distance range (78°~81°), both time-distance curves (b) and vespagram (c) might be misled. Red arrow in the vespagram (c) might be misinterpreted as the phase S660P. Absolute values after 4^{th}-root stacking are used to plot the contours in vespagram.

2.2 Topography of major discontinuities

2.2.1 Topography of 660-km discontinuity

For data in the azimuth range of 45°~135°, S660P converted oceanward of the slab was observed in 4th root stacks of 22 events (Fig. 5a and Table 3). Based on depth

contours of the subducting Pacific plate [*Gudmundsson and Sambridge*, 1998], our study area was divided into three regions (I, II and III in Figure 5a). They are the southern Kuriles (region I), Japan Sea (region II) and Izu-Bonin trenches (region III), respectively. The average time residual of S660P in region III is -0.7 s, which equates to a 7 km decrease in the depth of the 660. In regions I and II, average residuals are positive, indicating a deepened 660 (Table 2). However, as discussed above, considerable error may be introduced by inaccurate focal depth estimates. To combat this, we relocated events by minimizing the difference in the arrival times between direct P and pP phases of observed and synthetic seismograms in a least squares sense. We called the events as "marginal events" if their depth phase pP in teleseismic data (30º~90º) was unclear. Focal depth correction does not substantially change our results for region II which is within a km of the global mean. Depths estimates for regions I and III are reduced by relocation, moving to uplifts of 6.5 and 9.8 km, respectively (Fig 5b and Table 2, values in brackets for which marginal events were excluded from the averaging). While we are limited to only three regions to draw inferences from, we note that the two more steeply dipping subduction regions (I and III) have an elevated 660 and that the steeper the dip of the slab, the shallower the 660 beneath the slab.

To compare 660 topography between oceanward and landward sides of the slab, data from the same events but recorded in the azimuth range (225°~325°) were examined. On average, 660 is about 6~10 km deeper landward of the slab in Southern Kuriles (I) and Izu-Bonin Trench (III) regions. The negative Clapeyron slope of the ringwoodite disassociation results in a deeper 660-km discontinuity in cold areas. Since the converted

points at the 660 in the azimuth range of 225°~325° are in the slabs, we expect a deepened 660 in the landward direction. Region II (Japan Sea) doesn't follow this prediction (Table 2). One possible explanation for this apparent discrepancy is the frequently bimodal or otherwise complex nature of the stacked S660P phases in this region (Fig. 5c). For instance, the time residual for event 2002.09.15 in north China is -1.15 s but the stack waveform around S660P is complicated (Fig. 5c) compared with the stack in oceanward direction (Fig. 5b), and, indeed, we obtain substantially larger bootstrapped-derived standard deviations for the landward azimuth range (Table 3). Excluding this event and one other (1993.01.19) which had fewer than 10 traces in the stack and large uncertainty (>0.5 s in Table 3), the average residuals in Region II were comparable in both directions.

Table 2

Average time residuals and depth perturbations in three different regions

Average time residual	Region I	Region II	Region III
S660P (Fig. 5a)	0.5s (0s)	0.3s (0.186s)	-0.7s (-0.625s)
S660P_relo(Fig. 5b)	-0.1s (-0.65s)	0.267s (0.071s)	-1.107s (-0.983s)
S660P_az (Fig. 5c)	0.286s (0.342s)	-0.094s (-0.207s)	-0.358s (-0.38s)
Depth perturbations	Region I	Region II	Region III
S660P (Fig. 5a)	5.0km (0.0km)	3.0km(1.86km)	-7km(-6.25km)
S660P_relo(Fig. 5b)	-1km (-6.5km)	2.67km(0.71km)	-11.07km(-9.83km)
S660P_az (Fig. 5c)	2.86km(3.42km)	-0.94km(-2.07km)	-3.58km(-3.8km)

Average time residuals and depths perturbations in brackets are calculated by events except poor relocation (white triangles in Figure 5).

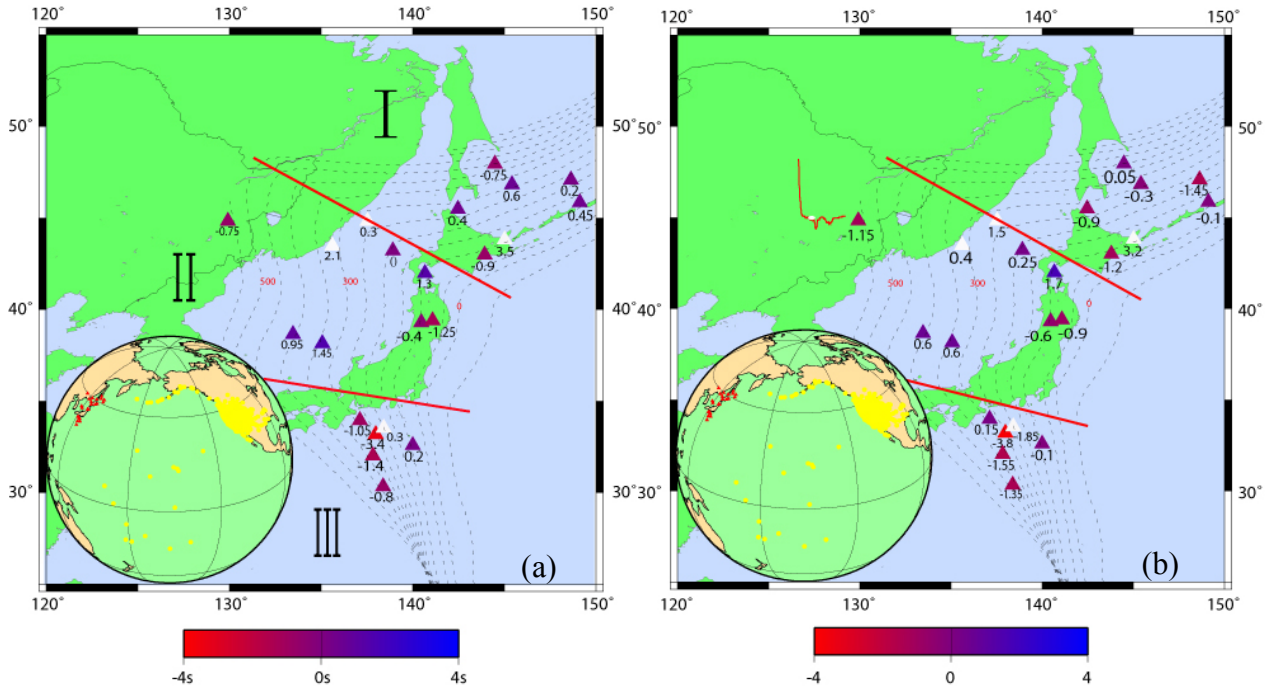

Figure 5 *(to be continued)*

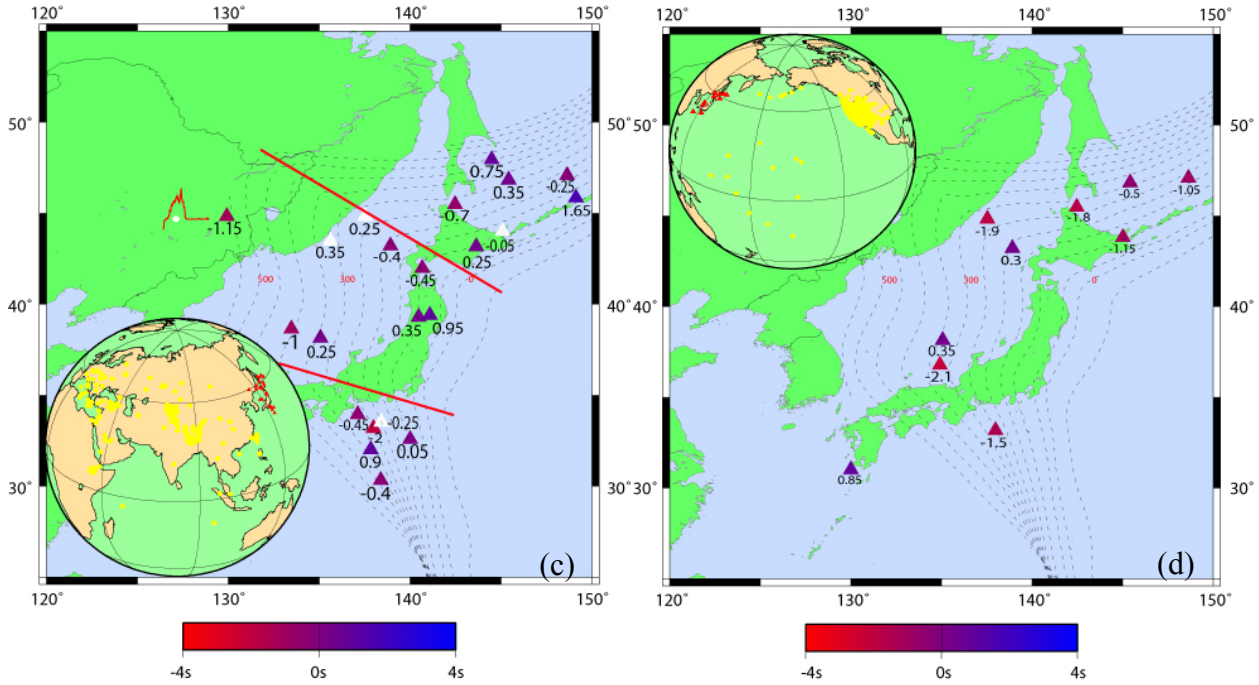

Figure 5: Time residuals of the converted phase at the 660 (a, b and c) and the 410 (d) in northwestern Pacific. Colored triangles represent time residuals (seconds) of stacking results for each event while white triangles denote events with little available depth phase pP seismograms for relocation. Both results before (a) and after relocation process (b) of the oceanward 660 (azimuth range: 45°~135°) are shown. Residuals (c) of converted points at the landward 660 (azimuth range: 225°~325°). Depth contours (black dash lines) of the subducting Pacific plate (Gudmundsson and Sambridge (1998) are plotted. Three sub-regions are divided based on the geometry of depth contours (red lines in a, b and c). Insets show events (red triangles) and stations (yellow dots). Example 4th root stacking waveforms (white dot denotes theoretical arrival time for S660P) for Event 2002.09.15 are plotted in b and c.

Table 3
Events used for obtaining time residuals of the oceanward S660P (azimuth range: 45°~135°), the landward S660P_az (azimuth range: 225°~325°).

Event	Latitude (°N)	Longitude (°E)	Evdp (km)	Evdp* (km)	Residual S660P(s)	Residual* S660P(s)	Traces	Std	Residual* S660P_az	Traces	Std	Res_NA S660P
1992.06.16	45.49	142.47	330	317.6	0.4	-0.9	31	0.500	-0.7	17	0.440	-0.9
1992.08.11	43.49	135.62	359	342	2.1	0.4	10	0.330	0.35	8	0.770	0.4
1992.08.24	41.98	140.66	120.5	124	1.3	1.7	37	0.200	-0.45	13	0.210	1.7
1992.08.29	33.19	137.98	289.4	286.4	-3.4	-3.8	18	0.088	-2	11	0.320	-3.8
1993.01.19	33.64	133.46	448.3	444.3	0.95	0.6	7	0.556	-1	11	0.680	0.6
1993.10.11	32.02	137.83	350.7	349	-1.4	-1.55	29	0.354	0.9	23	0.092	-1.5
1995.03.30	44.84	137.54	319.4	329	0.3	1.5	18	0.880	0.25	24	0.384	1.15
1995.03.31	38.15	135.06	365	357	1.45	0.6	48	0.190	0.25	32	0.450	0.55
1995.07.07	33.95	137.12	324	336	-1.05	0.15	46	0.447	-0.45	29	0.320	0.2
1995.07.29	30.34	138.38	435.6	430	-0.8	-1.35	36	0.258	-0.4	29	0.327	-1.35
1996.12.22	43.21	138.92	227	229.5	0	0.25	33	0.114	-0.4	26	0.065	0.25
1997.10.26	39.3	140.46	133.6	131.6	-0.4	-0.6	57	0.375	0.35	17	0.760	-0.7
1997.11.15	43.81	145.02	161	158	3.5	3.2	39	0.520	-0.05	13	0.497	2.9
1998.02.28	33.54	138.42	312	291	0.3	-1.85	19	0.790	-0.25	18	0.672	-1.85
1998.07.07	32.58	140	112.7	109.7	0.2	-0.1	32	0.600	0.05	6	1.166	-0.1
1998.08.18	45.85	149.12	116	111	0.45	-0.1	32	0.362	1.65	82	0.590	0

1999.05.12	43.03	143.84	102.7	99.7	-0.9	-1.2	81	0.086	0.25	83	0.524	-1.2
2000.07.10	46.83	145.42	359.6	350.8	0.6	-0.3	119	0.059	0.35	89	0.203	-0.2
2001.10.03	47.08	148.63	284.5	269.1	0.2	-1.45	85	0.175	-0.25	63	0.328	-1.5
2001.12.02	39.4	141.09	123.8	127.2	-1.25	-0.9	72	0.470	0.95	70	1.030	-0.95
2002.09.15	44.83	129.92	586.3	582	-0.75	-1.15	83	0.146	-1.15	109	0.466	-0.85
2004.11.07	47.95	144.48	474	482	-0.75	0.05	67	0.510	0.75	120	0.197	0.05

Evdp* and Residual* are the focal depth and time residuals after relocation, respectively.

Traces are the number of seismograms used for linear stacking.

Std represents bootstrapping estimated standard deviaion.

Res_NA represents the residuals using stations only in North America after relocation.

The stacking results from contrasting azimuth direction for the S660P demonstrate, to some extent, the feasibility of stacking data over a large distance range. The generally deeper 660-km discontinuity in the landward stacks is associated with colder temperatures at the conversion points of S660P. However, it would be inappropriate to deduce the temperature difference between cold slabs and the region under slabs from these average topographic variations. In our study, the difference of average depth of the 660 between oceanward and landward sides is on the order of 10 km and substantially smaller than previous studies [*Li et al.*, 2000; *Li and Yuan*, 2003; *Thirot et al.*, 1998; *Tono et al.*, 2005]. For example, in the coldest slabs of the northwest Pacific, a 20 to 40 km depression of the 660 was seen in the receiver function study [*Li et al.*, 2000]. Our

smaller estimates are not unexpected. Because of the large distance range of our data, S660P conversion points are spread over a large area, averaging a greater range of temperatures associated with the steep thermal gradients within the slab and reducing the maximum topography we are able to see. Moreover, use of a 1D reference model will emphasize areas where the 660 is flat--conversions from an inclined discontinuity will not follow the predicted travel time trajectory over a wide distance range--, again drawing the result away from the cold slab core. Our results agree fairly well with those of Li et al. [2008] who followed a largely similar method but with smaller aperture array data. While we suspect we are underestimating topography variability on both sides of the slab, we believe our results are stable and significant, especially on the oceanward side where slab-generated thermal gradients are much smaller. Last, because of complicated temperature and composition conditions in the subduction zone, the 660 was revealed a large variation by other previous studies [*Li et al.*, 2008; *Zang et al.*, 2006]. This is consistent with our result, which shows the depth of the 660 (Fig. 7) beneath slabs may vary up to ~40 km at some local places. Besides, recent numerical modeling implied complex slab geometry alone could result in isolated hot areas [*Lowman et al.*, 2007].

Because most stations for the oceanward study are in North America, the piecing points of the S660P at the 660 are focus in a small area (Fig. 5a). This small area of the piecing points can provide the relatively consistent polarity for stacking. To demonstrate the insignificant influence of the scatter stations out of North America, we choose the stations only deployed in North America (Fig. 6) for the oceanward 660 study with the same method and events. The maximum residual difference of the narrow S660P is 0.35s

(Table 3). The small variance of the differences (0.017 second) demonstrates, in this study, a larger azimuth range (45°~135°) for the S660P stacking is feasible.

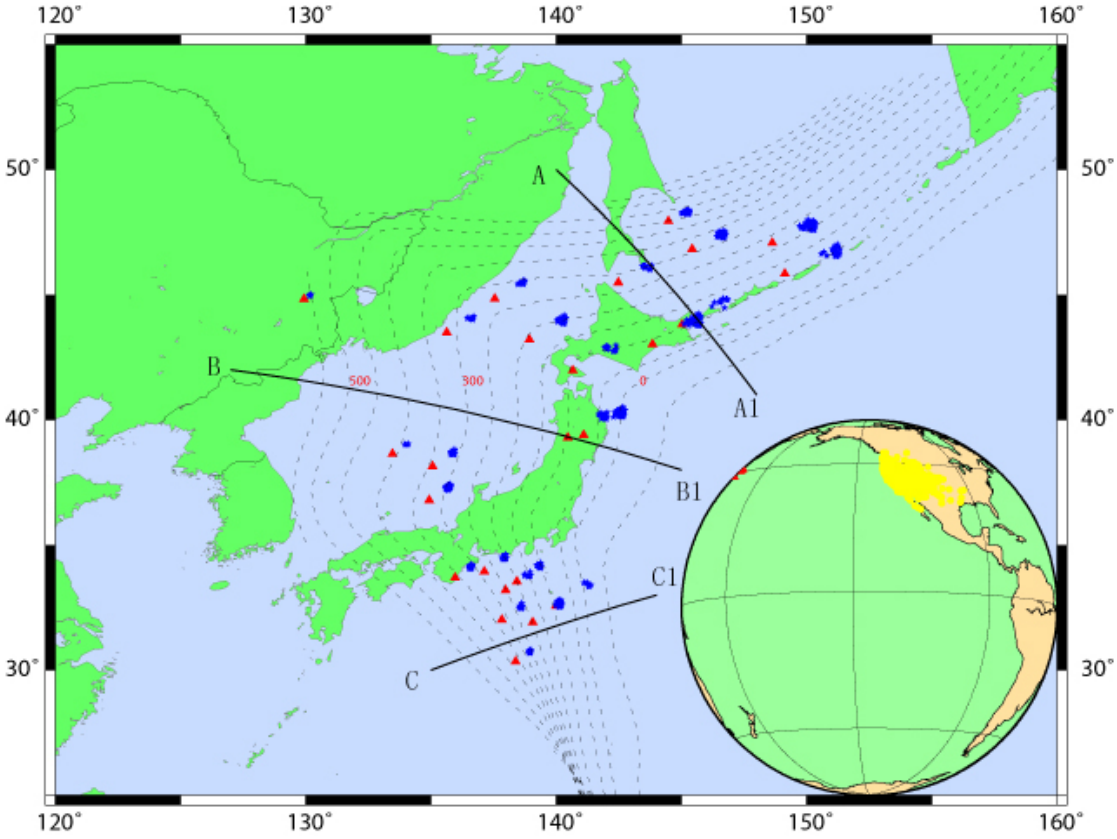

Figure 6: Narrow the azimuth range by only using the stations in North America. The red triangles represent the used events. Blue points are the piece points for the S660P on the 660. Three profiles (AA1, BB1, CC1) are drawn for the projection.

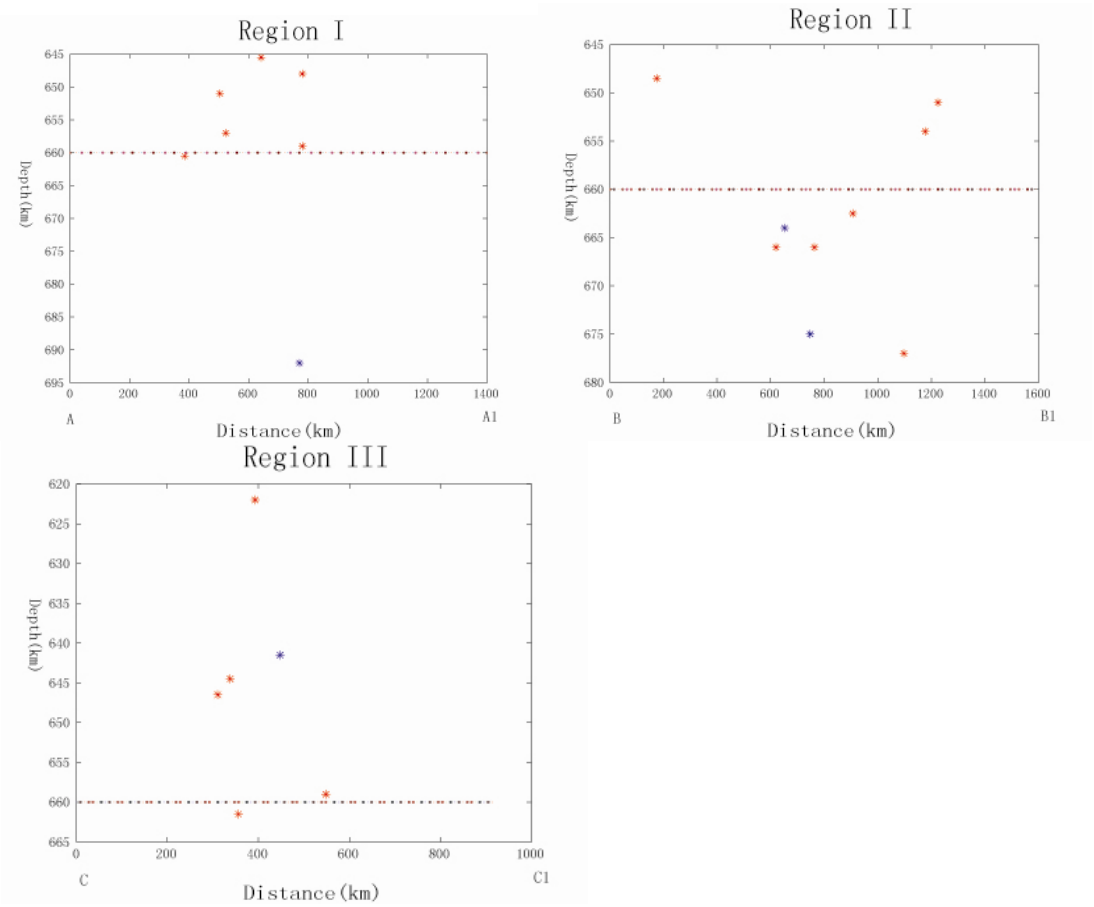

Figure 7: Orthogonal projection of the 660. Depths (red stars) of the 660 for each event after relocation, constrained by the S660P study, are projected along three profiles (AA1 for region I, BB1 for region II, CC1 for region III in Figure 6). Blue stars represent marginal events.

For Mariana and Tonga-Fiji, the azimuth ranges for the oceanward 660 study are 45°~135° and 35°~135°, respectively (Fig. 8). After relocation process, the average residuals for Mariana and Tonga-Fiji are -1.15s and -0.64s. The S660P results in Mariana and Tonga-Fiji also show the 660 beneath subducted slab is uplifted. And the average topography of the 660 beneath subducted slab in Mariana is shallowest. Again this result strengthens the deduction in northwest Pacific—the oceanward 660 is shallower as the dip angle of the subduction slab become larger.

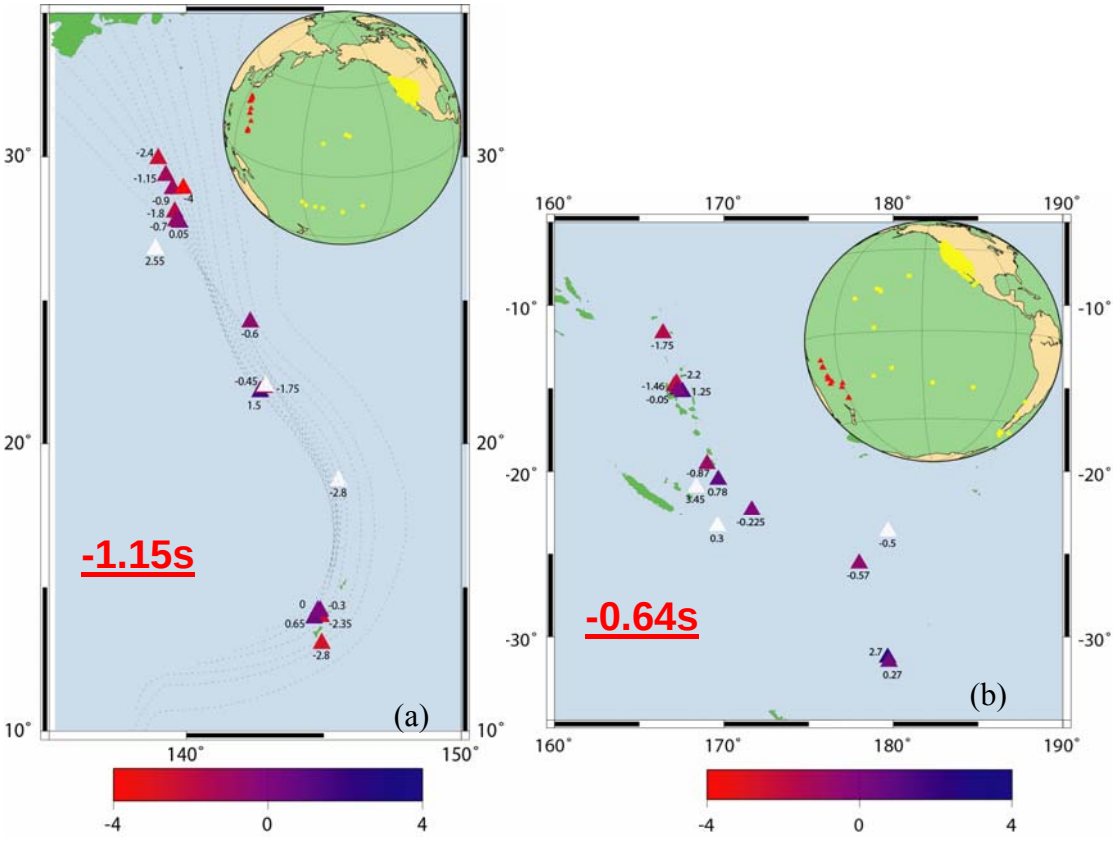

Figure 8: After relocation, time residuals of the converted phase at the 660 in Mariana (a) and Tonga-Fiji (b). Mean residuals (red number) except marginal events are shown.

2.2.2 Study of the 410 and the 520 discontinuities

We obtained only 10 events with useful stacks of S410P. While amplitude of the converted phases might play a role, we would expect fewer stacks as there were fewer events at depths $\geqslant$ 100 km but shallower than the 410 by a great enough margin to separate S410P from direct P. The majority of the residuals are negative indicated a regionally uplifted 410 (Fig. 5d and Table 4). However, in the eastern azimuth range (45°~135°), the probable cause of the uplifted 410 differs from that of the shallow 660 in Regions I and III (Fig. 5b). If we assume the thickness of cold slab is 100 km and subduction dip is 45°, then the distance between the hypercenter and the conversion point needs to be larger than approximately 100km/sin(45°)=141 km for the conversion to occur outside of the slab. As a matter of fact, 141 km is a safe estimation if small outgoing angle of the ray is considered. For example, if the outgoing angle is 15°, the gap between the hypercenter and the 660 requires 100km/sin(30°)*cos(15°)=193 km to convert beneath the slab. Most of our events are deeper than 270 km (Table 4), such that conversion points for the 410 are within the slab, not below it (or east of it) as in the case of the 660. As a result, the uplifted 410 in this study is a consequence of the positive Clapeyron slope of the olivine to wadsleyite transition and depressed slab temperatures at the 410. Conversion points for S660P for the azimuth range of 45°~135° (Fig. 5b) are almost all outside the slab. For this reason, we didn't compute transition zone thickness as was done in previous studies [*Gu and Dziewonski*, 2002; *Lawrence and Shearer*, 2006; *Lebedev et al.*, 2003; *Li et al.*, 2000]. Nevertheless, since the topographic variations of the 410 obtained in this study are reasonable and consistent with mineralogical results, it

again demonstrates that large aperture array stacking is capable of revealing topography of discontinuities in the transition zone.

Table 4
Events used for obtaining time residuals of phase S410P

Event	Latitude (°N)	Longitude (°E)	Evdp (km)	Evdp* (km)	Residual (Second)	Residual* (Second)	Traces	Std
1992.06.16	45.49	142.47	330	317.6	-1.9	-1.8	19	0.429
1992.08.29	33.19	137.98	289.4	286.4	-1.2	-1.5	18	0.630
1995.03.30	44.84	137.54	319.4	329	-2.9	-1.9	17	0.680
1995.03.31	38.15	135.06	365	357	1.1	0.35	16	0.390
1996.12.22	43.21	138.92	227	229.5	0.05	0.3	29	0.15
1997.11.15	43.81	145.02	161	158	-0.9	-1.15	39	0.456
2000.07.10	46.83	145.42	359.6	350.8	0.4	0.4	119	0.16
2001.10.03	47.08	148.63	284.5	269.1	0.95	0.65	85	0.489
2005.11.21	31.02	130	145	149	0.25	0.85	113	0.215
2007.07.16	36.79	134.92	362.8	358.4	-1.65	-2.1	368	0.067

The 520-km discontinuity (hereafter called the 520) is generally regarded as the seismic expression of the transition between wadsleyite and ringwoodite. It is commonly observed in studies of long-period seismic data [e.g., *Flanagan and Shearer*, 1998; *Shearer*, 1991a; *Revenaugh and Jordan* 1991] and frequently absent in short-period

studies [*Benz and Vidale*, 1993] suggesting that its two-phase interval varies considerably. Mineralogical experiments show that it could be as great as 60 km thick under anhydrous conditions [*Akaogi et al.*, 1989] and sharpening to 15 km or less with increased water [*Inoue et al.*, 1995]. Seismic visibility of this discontinuity can thus provide a constraint on water distribution in the mantle transition zone. It should be less affected by slab dehydration beneath subducting slabs where its visibility may be more reflective of normal mantle. Region I was selected to study the 520 because available events are best distributed in this region. Unfortunately no clear signal of S520P could be found by 4th root stacking. Large topographic variation of the 520 and/or the wide two-phase interval expected in anhydrous environments might both lead to a lack of observations. The velocity contrast of the 520 is smaller than either the 410 or 660, so perhaps S520P is simply falling below the noise level in our data. Further study of S520P by other methods (e.g. double array stacking in [*Hutko et al.*, 2008]) might be useful to investigate the sharpness of the 520 in this region and shed light on water content in mantle transition zone.

2.3 Discussion and conclusions

Topographic variation of the 660 beneath subducting slabs mirrors subduction dip and geometry of slabs above the 660. Under the Japan Sea (Region II), there is little difference in average depth of the 660 between the landward and oceanward sides. This suggests that the cold slab above the 660 did not significantly lower the temperature at the 660-km discontinuity. In addition, the 660 in both directions is very close to the

global mean (~660.7 km oceanward, ~658 km landward). Regional and global tomography [*Fukao et al.*, 2001; *Van der hilst et al.*, 1991; *Zhao et al.*, 1994] show the subducting slab under Japan Sea is subhorizontally deflected within the transition zone. While, under the Southern Kuriles (Region I) and Izu-Bonin trenches (Region III), deeper landward 660 suggest cold slabs penetrating into lower mantle and dramatically changing temperature around the 660.

The uplifted 660 in oceanward direction under the more steeply dipping Southern Kuriles (~653.5 km in region I) and Izu-Bonin trenches (~650.2 km in region III), suggest that subduction dip may relate to the topography of the 660 beneath subducting slabs. In order to understand what might link topography of the 660 changing with the dip of subducting slabs, we first consider thermal anomalies and chemical composition. If we only consider the disassociation of ringwoodite (i.e., if we ignore the non-olivine components) and use the Clapeyron slope of -2.0 MPa/K for the 660 [*Vacher et al.*, 1998], a ~10 km topographic variation requires a thermal anomaly of ~180 K. Applying this to regions II and III suggests that Izu-Bonin is ~180 K hotter than the Japan Sea region at 660 km depth. Such a perturbation in temperature would be consistent with low velocity anomalies imaged beneath subducting slabs in recent seismic studies [*Obayashi et al.*, 2006; *Wang and Chen*, 2009; *Zhao et al.*, 2007]. Two possible mechanisms have been proposed for the low velocity anomalies in the mantle transition zone: a rising hot plume from the lower mantle [*Obayashi et al.*, 2006; *Wang and Chen*, 2009] or a sinking hot anomaly entrained by the downgoing slab [*Honda et al.*, 2007]. Based on the shape of the low velocity anomaly in tomographic images, Honda et al. [2007] proposed it was the

result of a hot anomaly produced in the Pacific superplume area and carried beneath the northwestern Pacific by the high viscosity slab. In this scenario, a more steeply dipping slab reduces the distance between the 660 conversion point and the entrained hot material, elevating the 660 locally, perhaps explaining the shallower 660 in Regions I and III. The same geometric arguments would hold for a plume ascending along the base of a dipping slab.

Trench retreat has been proposed to interpret seismic observations in the northwestern Pacific [*Li et al.*, 2008; *Long and Silver*, 2008; *Miller and Kennett*, 2006]. To the extent that this is happening, it should depress the 660 because as the trench retreats, shallow (i.e., cold) mantle is forced downward, lowering temperature at the 660. Complex slab geometry alone can result in isolated hot areas [*Lowman et al.*, 2007] but without further modeling, it is not clear if conditions are right in the northwestern Pacific to produce hot bodies landward of the slab.

The transition zone is a possible water reservoir because of the high water solubility of wadsleyite and ringwoodite relative to olivine and perovskite [*Bercovici and Karato*, 2003]. The presence of water has been frequently invoked to explain seismic anomalies around the mantle transition region [*Schmerr and Garnero*, 2007; Song et al., 2004]. Near the 660, wet conditions would expand the stability field of ringwoodite to higher pressures and therefore depress the 660 [*Ohtani and Sakai*, 2008]. Litasov et al. [2005] found that 2 wt% water in hydrous peridotite led to a 0.6 GPa increase in the disassociation of ringwoodite (~15 km deeper for the 660) over dry peridotite at 1473° K. Dehydration processes can strongly influence hydration above downgoing slabs, but the

landward side should be shielded unless hydrated material is able to flow around the slab or if slab hydration extends to much greater depths than currently thought. Drier conditions beneath subducting slabs would reduce the depth of the 660. We don't, however, believe this is the source of the elevated 660 in Regions I and III. First, ~10 km of topographic variation would require a ~1.3 wt% water contrast between the oceanward portions of the Izu-Bonin and Japan Sea subduction zones, which contradicts a relatively dry mantle transition zone (<0.2 wt% water) revealed by electrical conductivity studies [*Huang et al.*, 2005; *Yoshino et al.*, 2008]. Second, to the extent that oceanward 660 topography does indeed mirror slab dip, we know of no relation between slab dip and water content.

Major element chemistry also affects phase transition pressure. In this regard, the two most important elements to consider are Fe and Al. Because the addition of 1 mol.% Fe only causes a depth change of 0.13 km for the 660 [*Sinogeikin et al.*, 2003], highly implausible variability in Fe content would be required to explain our observations. The phase transformations of non-olivine component system, such as from garnet to perovskite, complicate seismic structure near the 660. For example, double discontinuities [*Ai et al.*, 2003] and velocity gradient variations [*Wang et al.*, 2008] have been attributed to the non-olivine component. Al couples the olivine pyroxene portions of the transition zone. The addition of Al deepens the 660 but whether the effect is large enough is questionable and, again, there shouldn't be a link to subduction dip.

By stacking S waves converted to P by source-side transition zone discontinuities, we investigated topographic variations of the 410 and 660 above and below subducting

slabs in the northwestern Pacific. The deeper landward 660 and the shallow 410 observed at stations landward of the slab are consistent with mineral physics and generally colder conditions in or near the slab.

Oceanward of the slabs, the situation for the 660 is reversed. If local temperature is governed by the slab alone, we would expect a depressed discontinuity in Regions I and III where the more steeply dipping slab results in conversion points closer to the cold slab anomaly. What we observe is a 10 km uplift in Region III beneath the Philippine Sea and a 6.5 km uplift in the Kuriles. Region II, beneath the Japan Sea is within error of the global mean. In Mariana and Tonga-Fiji regions, the average residuals beneath subducting slabs also indicates the relationship between the topography of the 660 and the dipping angles of the slabs. We suggest that low velocity anomalies imaged beneath subducting slabs, perhaps due to entrainment of hot material emplaced at shallow depths oceanward of the trench or hot material rising along the bottom edge of a downgoing slab, extend to the 660 and produce local elevation. The greater subduction dip in Regions I and III where uplift is noted would move the hot material closer to the S660P conversion point maximizing its effect.

Chapter 3, Seismic velocity anomalies

Triplication waveform modeling is frequently used to constrain seismic structure around transition-zone discontinuities. Beneath northern Eurasia, the velocity increase across the 660 is only about 50% of the value predicted by the IASP91 model [*Ryberg et al.*, 1998]. In the northwestern Pacific, high-velocity anomalies associated with the depressed 660 are interpreted as the influence of the cold subducting slab [*Tajima and Grand*, 1995; 1998]. On the contrary, denser data constrain depth-averaged ~1.5% P and ~2.5% SH low-velocity anomalies in the depth range of 560–760km, which are explained by a 350–450K temperature variation beneath subducting slab [*Wang and Chen*, 2009]. Beneath Fiji, low-velocity anomalies and anisotropy of shear waves are taken as evidence for a large scale remnant of slab [*Chen and Brudzinski*, 2001]. Recently, both P [*Wang and Niu*, 2010] and SH wave [*Ye et al.*, 2011] studies of triplication waveform modeling suggested a broad 660 km discontinuity beneath northeast China. To avoid the influence of shallow structure and keep the source time function to be simple, deep events (>100 km) are often selected for triplication waveform modeling. Deep earthquakes (>100 km) overwhelmingly occur in subduction zones. High quality receivers for typical triplication distance ranges (10º~35º) are usually only available on the continental side of subduction. As a result, most previous studies using triplication waveform modeling have sampled in subduction zones. However, in all the referenced studies, synthetic waveforms were calculated for a 1D layer model. Given the evident 3D nature of subduction, it is important to consider the limitations of 1D triplication waveform modeling in these complex regions.

3.1 Method and modeling results

Abrupt velocity increases with depth set up triplicated body wave arrivals (i.e., 3 separate arrivals at a single distance) whose timing and amplitude can be used to constrain discontinuity depth and width and velocity gradients near the boundary (see Fig. 9). The three seismic phases (Fig. 10) are: the wave propagating above the discontinuity (AB branch), the reflection off the discontinuity (BC branch) and the wave traveling below the discontinuity (CD branch). It is common to utilize forward modeling to obtain good fits to data while exploring seismic velocity model space. In previous studies, synthetics were calculated for 1D models. But lateral variation is large in subduction, due, at a minimum, to the low temperature of subducted slabs. For instance, regional tomography implies high velocity anomalies up to ~5% for cold slab [*Zhao et al.*, 1994; *Zielhuis and Nolet*, 1994]. Under such conditions, one would expect the geometry of subducted slabs and event-station pairs to affect wave propagation paths. The question is not if, but rather how strongly? We need to test how synthetics obtained by 1-D methods differ from 3-D methods of waveform modeling in order to meaningfully interpret studies using 1D methods. Given the costs of 3D seismic modeling, one wants to employ it only when necessary.

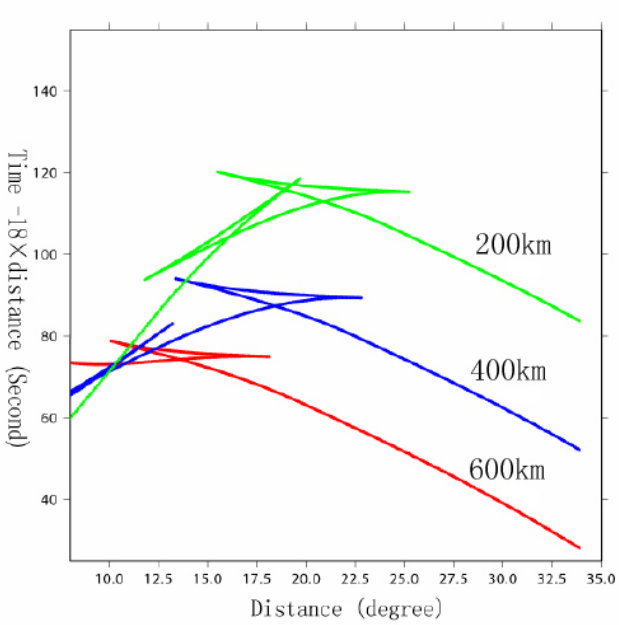

Figure 9: Travel time curves of triplications with different hypocentral depths. Two triplications appear when focal depth is less than 410km.

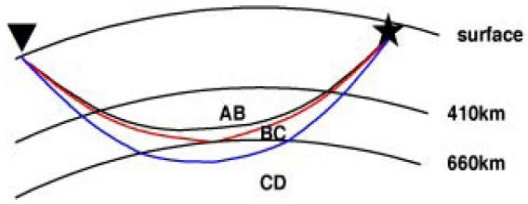

Figure 10: Raypaths of triplicated arrivals near the 660-km discontinuity. The source and station are represented by the black star and inverse triangle, respectively.

3.1.1 Comparisons between 1D and 3D method

For 1D method, our approach is similar to previous studies [*Tajima et al.*, 1998; *Wang and Chen*, 2009; *Wang et al.*, 2008]. We adopted a normalized square half-sinusoid wavelet as the input source time function in synthetic calculations. The focal mechanism used in this study is the same with event 2003208 from the Harvard centroid moment tensor (CMT) solutions (Table 5). A specified source (45ºN, 140ºE and 466 km) was given for comparison calculations. Synthetics were calculated with the above source information by using the reflectivity method [*Muller*, 1985; *Wang*, 1999]. In this section, we only compared the synthetics based on different models and did not used the real observations.

Table 5
Parameters for event 2003208

Event	Origin Date[a]	Origin Time (UT)	Latitude °N	Longitude°E	Depth (km)
2003208	27 Jul 2003	06:25:32.5[b]	46.98[b]	139.30[b]	466.2[b]
Magnitude m_b	Half duration (second)	Strike (°)	Dip (°)	Slip (°)	Scalar Moment
6.3[a]	5.5 [a]	61 [a]	44 [a]	158 [a]	1.46e+26 [a]

[a]Values from the Harvard centroid moment tensor (CMT).

[b]Hypercenters and origin times determined in this study.

To compute 3D synthetic seismograms, I implimented the spectral element method (SEM) of [*Komatitsch et al.*, 2002; *Komatitsch et al.*, 2010] on cluster computers at the

Minnesota Supercomputer Institute (MSI). In each SEM simulation, one full mantle wedge (90~150ºE, 25~55ºN) is divided into 32*16=512 slices. According to the SEM manual (page 29), the approximate shortest period is approximately equal to (256/NEX_XI)*(ANGULAR_WIDTH_XI_IN_DEGREES/90)*17. In our simulations, this allows calculations to be accurate down to periods as low as (256/512)*(60/90)*17=5.67s. The process of generating 3D velocity models is discussed in Appendix A. These models use PREM as a base, adding a shear-wave velocity perturbation point by point. Using 512 CPUs, a typical 3D calculation took about 3 hours. 1D and 3D calculations use the same source paramaters and assume a linear station array. Because the foccal depth (466 km) is deeper than 410km, there is only one triplication (Fig.10). This was done to simplify the investigation of the influence of subduction geometry.

As an initial benchmark test, both 1D and 3D methods were used to compute synthetics for the 1D PREM model. Synthetic data and travel-time curves for the three branches of shear waves turning near 660-km depth, calculated through TauP, are shown in Fig.11. The two methods produce similar results, although more Gibbs phenomena is apparent in the lower frequency resolution SEM synthetics. These minor differences are nearly eliminated by low-pass filtering of 1D results to match the SEM spectrum (Fig. 11b).

I designed two 3D models to test the influence of subduction zone geometry on triplicated arrivals. In model 1, raypaths are parallel to the trench (Fig.12b); in model 2, raypaths are perpendicular to the trench (Fig.12c). In both, we fixed the positions of the

source and stations as before but changed the subduction direction of the cold slab. The cold slabs have a 2% high velocity anomaly that dips at a constant 45º angle and is 100 km thick. The slab flattens atop the 660-km discontinuity instead of penetrating into lower mantle. For the parallel model, the synthetic results indicate that the AB branch arrives earlier in the distance range of 12.5º-18.5º (black lines in Fig.12a). While, in the perpendicular model, the AB branch arrives earlier from 15º to 25º (blue lines in Fig.12a). The differences of arrival times are dictated by how much of the raypaths is in the cold slab. For example, at small distances (e.g. 13º), the rays of AB branch arrivals follow the slab in the parallel model but leave the slab at the beginning in the perpendicular model. This leads to a faster AB in the parallel model (Fig.12a). In addition, I notice that the triplication waveforms of the two models are significantly different as well. Two clear spikes are obvious in the parallel model, especially for some distances (21º~25º) the later having larger amplitude. On the contrary, the later spikes in the perpendicular model appear much smaller than first arrivals (Fig.12a). These simple simulations demonstrate that not only travel time differences of the triplicated phases but also their waveforms are significantly affected by slab structure and geometry. It would be difficult to accurately extract discontinuity structure from 1D modeling of triplications, even for data confined to a narrow azimuth range. Therefore, the depth-average velocity structure around the discontinuities found by 1D methods should be cautiously considered.

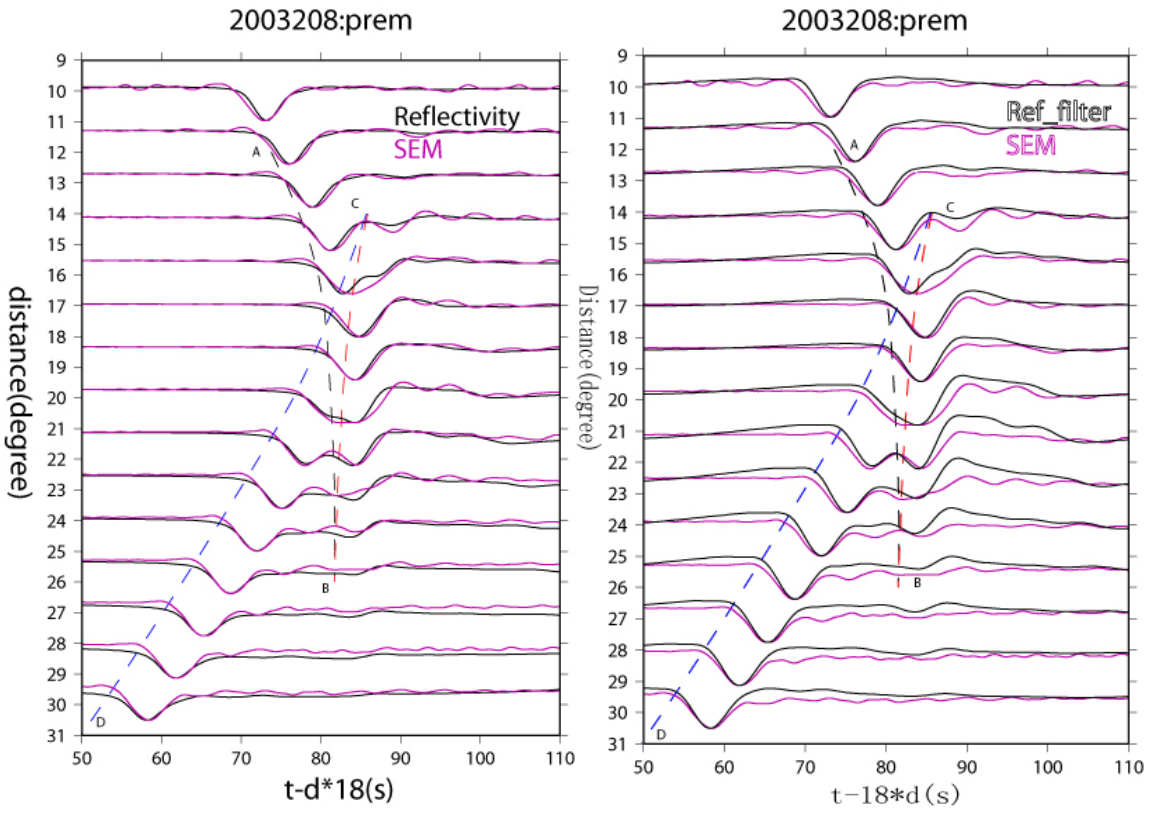

Figure 11: Comparisons of synthetics calculated by reflectivity method (black lines in a), its band-pass-filter (0.02~0.2Hz in b) and SEM for 1D PREM (red lines). Travel-time curves of the triplication (dash lines) are shown.

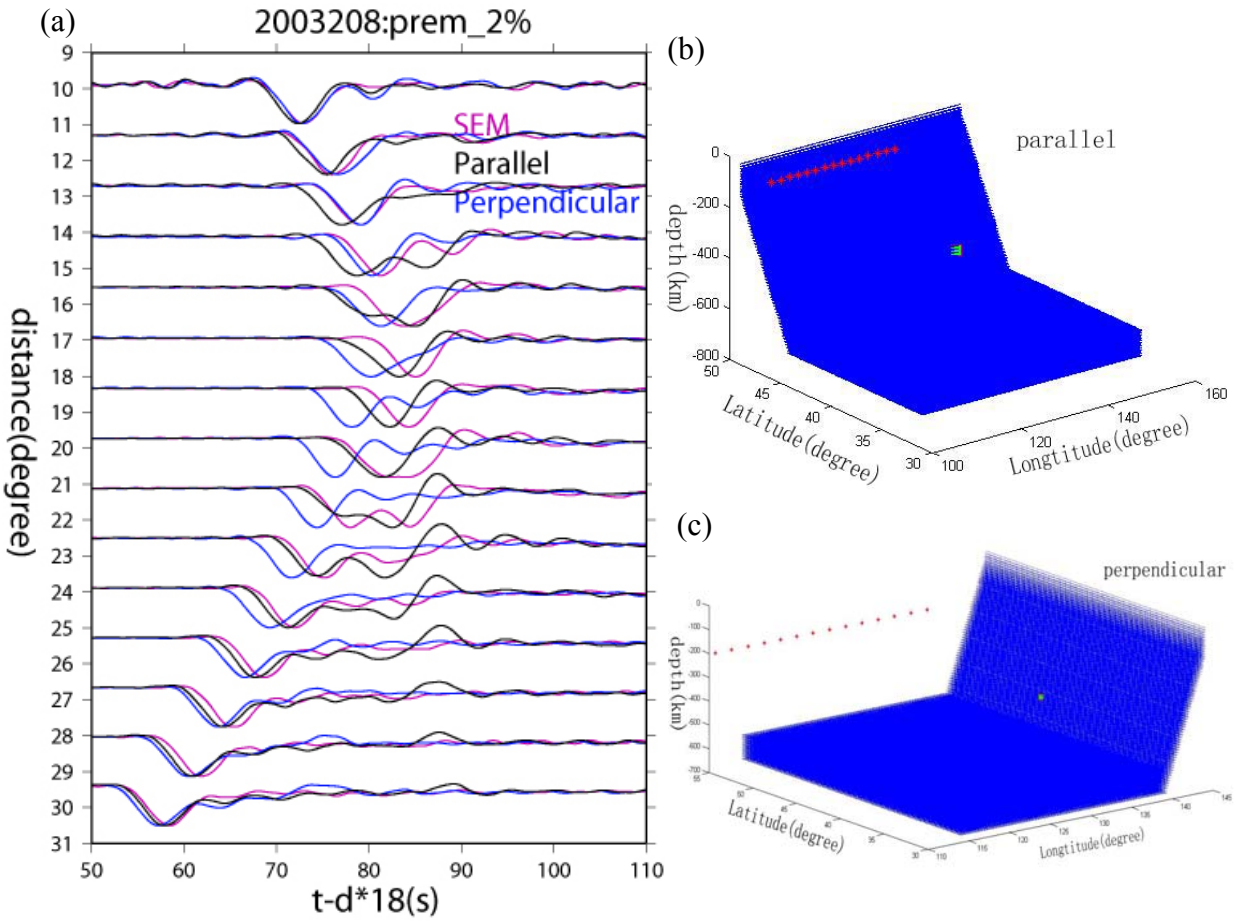

Figure 12: Comparisons of synthetics (a) calculated by SEM for 1D PREM (red lines) and two 3D models (blue lines for the perpendicular model and black lines for the parallel model). Stations (red dots), focus (green square) and 2% high velocity perturbation of the slab, relative to PREM, for the parallel (blue in b) and perpendicular (blue in c) models are shown.

3.1.2 3-D waveform modeling for event 2003208

Event 2003208 occurring in the Southern Kuril Islands was chosen for detailed 3D triplication waveform modeling. Waveform data for this event have very high signal-to-noise ratios as described in a previous study [*Wang and Chen*, 2009]. The data set I use comes from three different networks: 24 CSN (Capital Seismic Network) stations, 13 CDSN (Chinese Digital Seismic Network) stations, and 8 NCISP-III stations (Northern China Interior Structure Project) stations, spanning a distance range of 10º~35º, with the densest data from 15º to 21º. Except for station HIA, the azimuths of all the source-station pairs vary by no more than 15º. The 466-km focal depth for event 2003208) was improved through relocation by minimizing the arrival time difference of both S and sS phases (Appendix B). This assures that only one triplication exists in my waveform modeling, which may help better reveal the velocity structure around the 660-km discontinuity.

To standardize data from several networks, the instrument response was deconvolved from all trace. Because the source time function for this event is large (~11s), the influence of high frequency components to the waveforms is minor. In fact, spectral analysis of the S phase for this event indicated the main frequency components were concentrated in the range of 0.02~0.3 Hz. To retain the original waveforms as much as possible and compare with previous 1D study, all the seismograms were band-pass filtered from 0.02 to 4Hz during this process and no additional filtering was performed. I did not correct travel-times for individual stations because the intra-station time shifts appear small (<1 s) and show no obvious tendency over the distance range for this event.

Synthetics based on classic 1D model IASP91 [*Kennett and Engdahl*, 1991] were calculated and are compared with the observations in Fig.13a. Three elements of waveform mismatch are noticed. (1) For the distance range of 15º~17.5º, only one spike exists in synthetics. Two spikes are clearly displayed in observations and the later ones have comparable or greater amplitude. (2) Over the distance range of 19.5º~21º, synthetics show well separated triplication phases, which are much closer to each other in observed data. In addition, the first arrivals have smaller amplitude in observations. (3) Between 23º~29º, the cusp of the branch AB and BC disappears in our calculation, while the later phases are distinctly and consistently observed in data. We also tried several 3-D tomographic models, such as model jp3d1994 (Fig.13b) [*Zhao et al.*, 1994], s40rts (Fig.13c) [*Ritsema et al.*, 2011] and s362ani_3DQ (Fig.13d) [*Kustowski et al.*, 2008]. But none of them noticeably improve the mismatches in the 1D IASP91 model. This is likely caused by their limited lateral resolution and poor ray coverage around the 660 in this region, as well as damping which limits the size of the shear velocity perturbations.

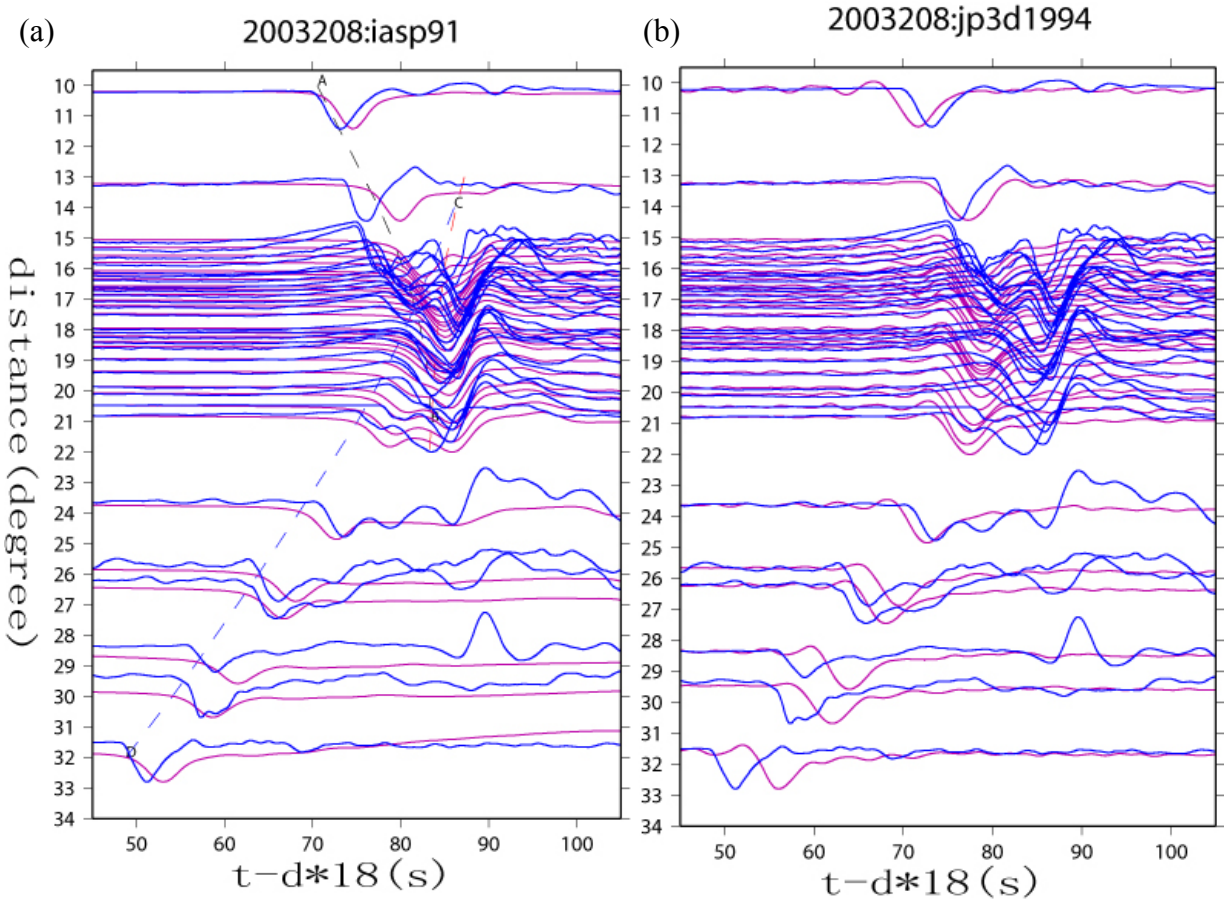

Figure 13: Comparisons of observations (blue lines) and synthetics (red lines) based on four models: (a) IASP91 [Kennett and Engdahl, 1991], (b) jp3d1994 [Zhao et al., 1994], (c) s40rts [Ritsema et al., 2011] and (d) s362ani_3DQ [Kustowski et al., 2008]. Trave-time curves of the triplicated arrivals are plotted for the 1D model IASP91.

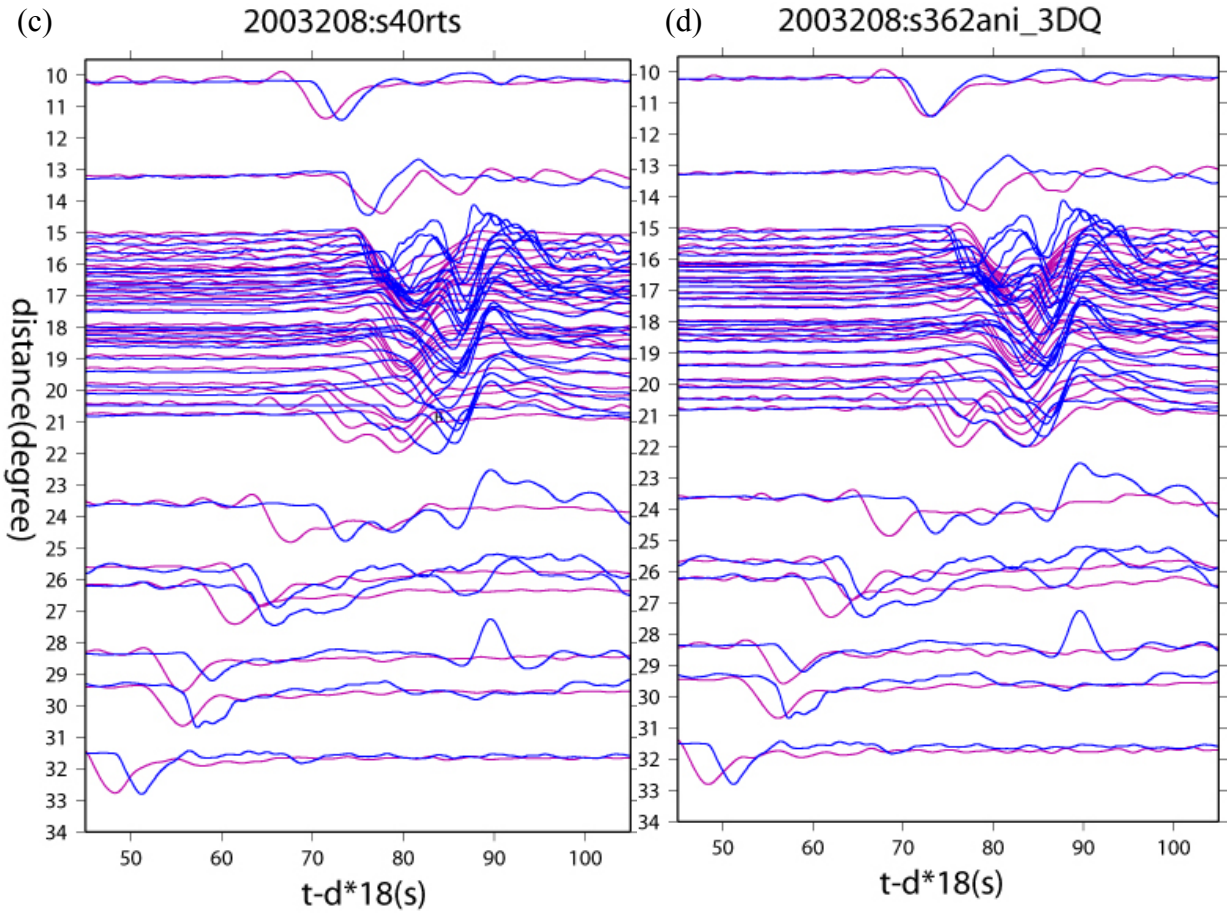

Figure 13 *(continued)*

To construct a 3D model with shorter wavelength slab structure than those obtained by tomography, I followed a simple process. I began with the depth contours of the subducting Pacific slab [*Gudmundsson and Sambridge*, 1998] as the top surface of the cold slab (Fig.14) and assumed that the bottom surface of the slab is approximately 141.4 km below that top. In this way, the thickness of the slab is approximately 100 km if the dip angle of the slab is locally 45 degrees. By varying the thickness of the slab and the magnitude of the high-velocity anomaly defining it in the 3D models, I generated a suite of candidate structures. Model "contour1" (Fig.15), with +5% high velocity anomaly and

100-km thick slab, matches observations better than IASP91 (Fig.16) or any of the tomographic models. In detail, "contour1" greatly improves the first mismatched element in the IASP91 modeling. Because a large part of AB branch propagates inside the high velocity slab, separation of the two initial spikes is big enough to fit the observations between 15º~17.5º. Although there is a trade-off between the thickness and the velocity anomaly of the slab, my trial-and-error modeling suggests a smaller velocity anomaly or thinner slab produces intervals for triplicated phases that are too small. For example, the contour2 model (+5% high velocity and 50-km thick slab) causes the two initial spikes of the synthetics to merge into a single broadened spike between 16.5º~17.5º (Fig.17).

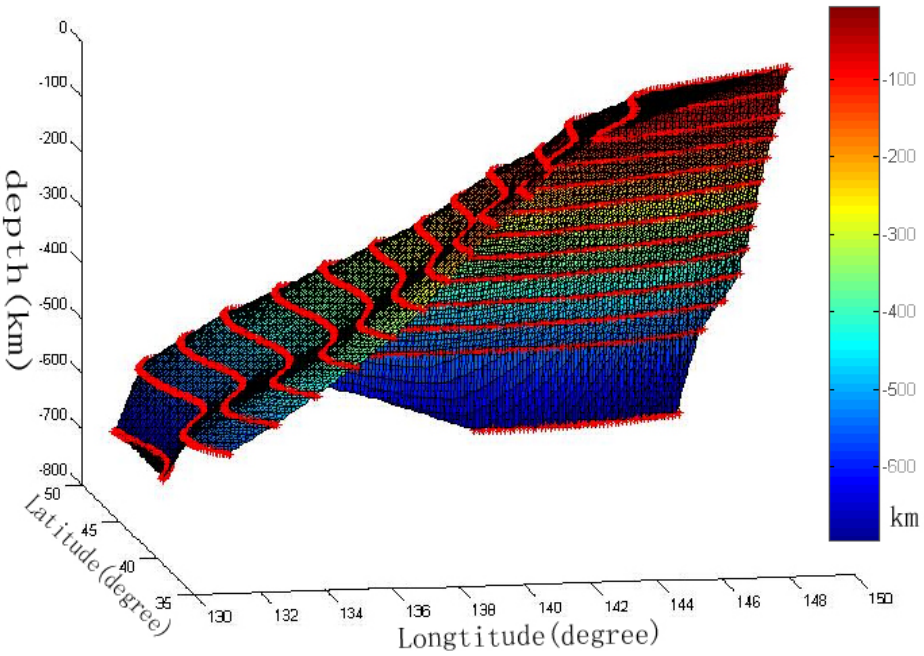

Figure 14: Using the depth contours (red lines) to reconstruct the top surface of the Pacific slab.

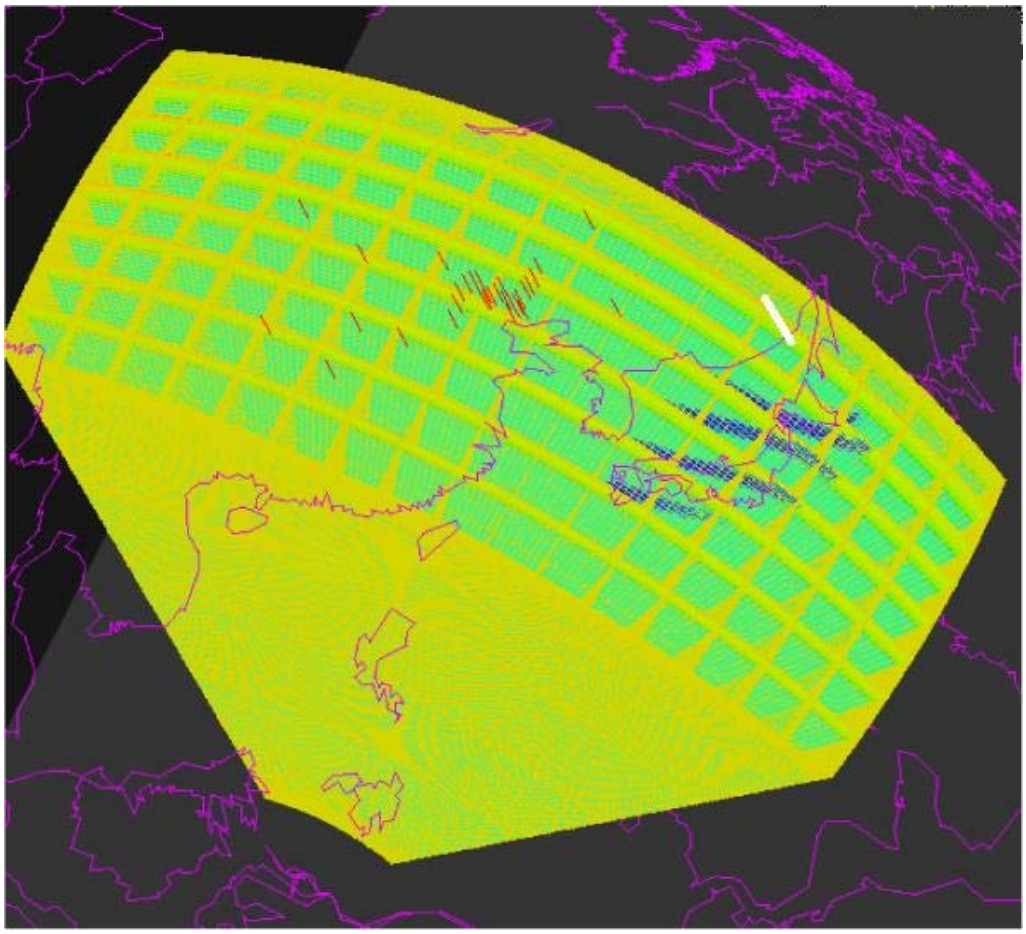

Figure 15: S-wave velocity model based on depth contour lines of the Pacific subducted slabs. Blue meshes represent 100km thick subducting slab with 5% high velocity anomalies. Coastlines (purple lines), stations (red bars) and the epicenter for event 2003208 (the white bar) are shown. The wedge in this schematic figure is subdivided into 16*8 slices (128 CPUs), which contains 32*16 slices (512 CPUs) in our SEM simulations. The center of the wedge is at (40^{o} N, 120^{o} E), and the lateral dimension is 30*60.

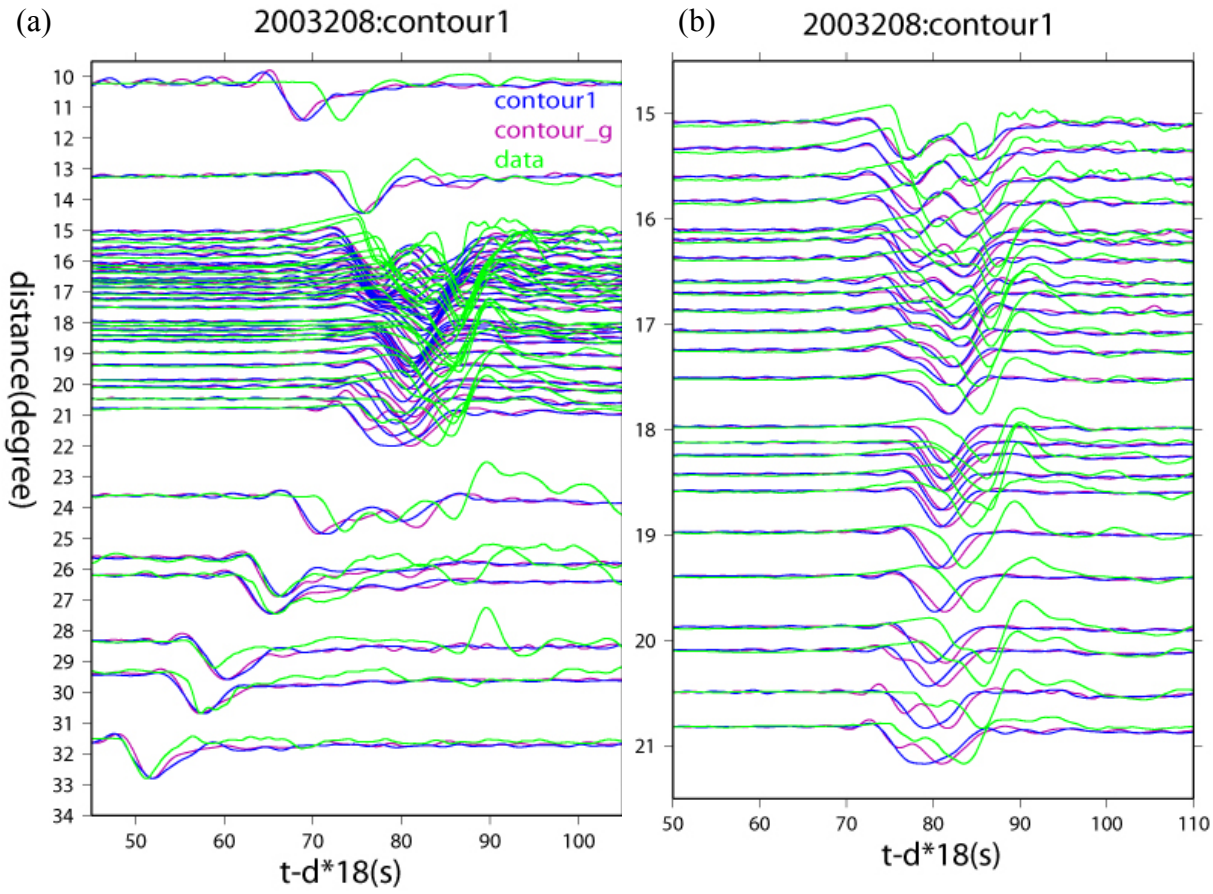

Figure 16: Comparisons of observed tangential displacements for event 2003208 (green traces) and synthetic waveforms calculated using the model contour1 (blue traces) and contour_g (purple traces). (b) is enlarged part of (a).

Nevertheless, mismatches of later phases at 19.5º~29º have not been eliminated yet for the "contour1" model. In order to slow the AB and BC phases, the "contour_g" model was designed. This model has structure identical to "contour1" above 560 km but removes the high velocity anomaly of the cold slab at deeper depths. Instead of high velocity anomaly, normal shear-wave between 560 and 660-km depth separates

triplicated phases at 19.5º~21º (Fig.16b). We also calculated the synthetics for a model which the high velocity anomaly terminated at 600 km. Although the differences between two models are tiny, the details of four waveforms around 20.5º for the "contour_g" model fit the observed data a little bit better. Even the synthetics for "contour_g" are consistently early through 15º ~20º, it is preferred though. This is because the structure near the discontinuity is sensitive to the relative time interval between triplicated phases and the absolute time could be affected by the shallow structure under stations and original time of the source.

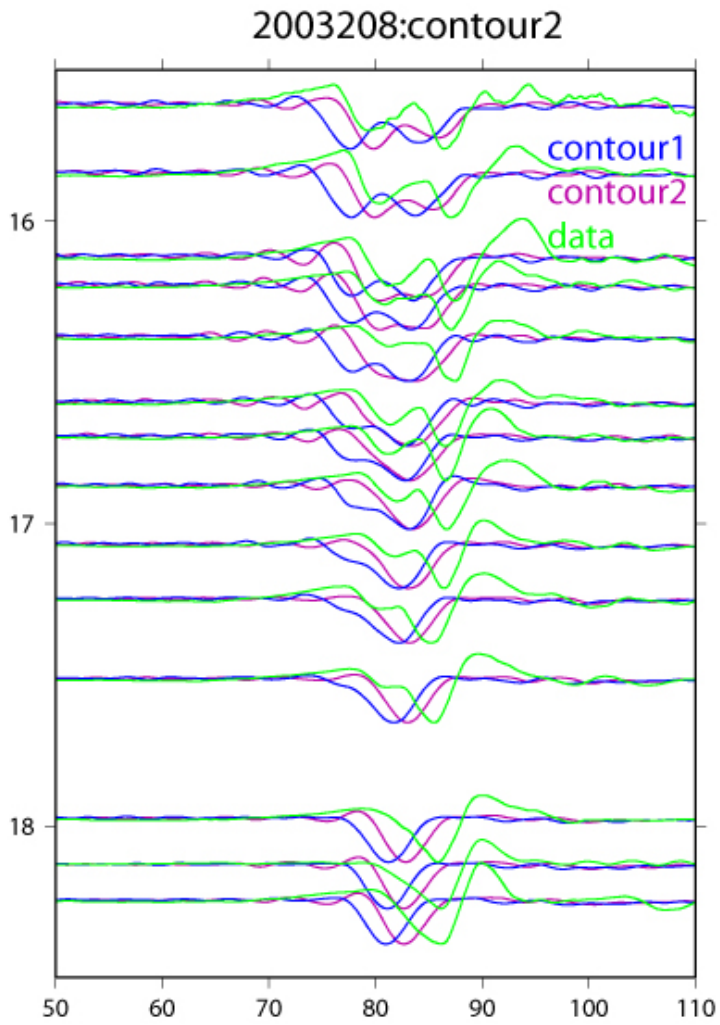

Figure 17: Comparisons of observed tangential displacements for event 2003208 (green traces) and synthetic waveforms calculated using the model contour1 (blue traces) and contour2 (purple traces).

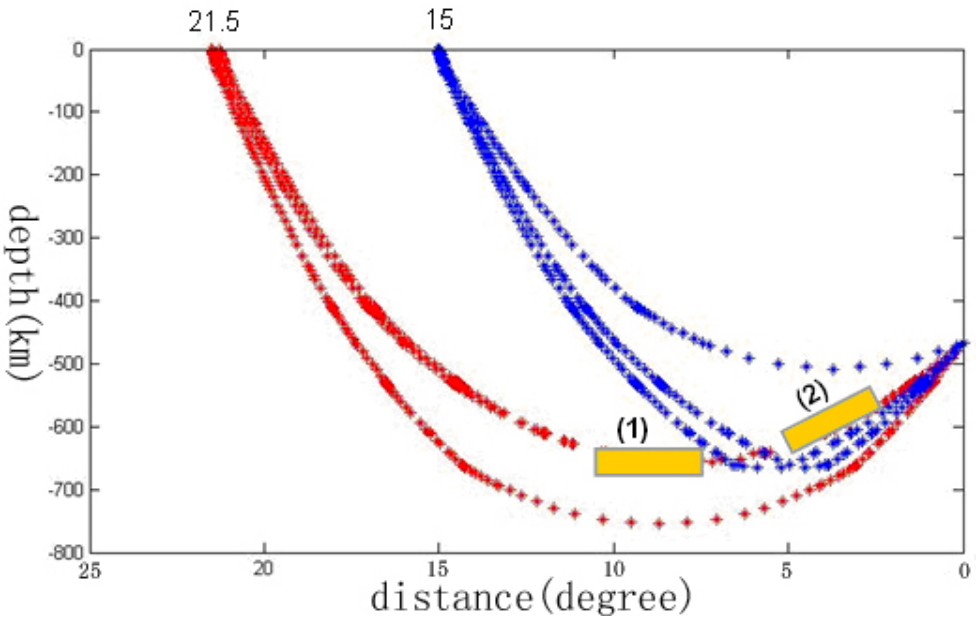

Figure 18: Raypaths of triplications for two distances: 15º (blue stars) and 21.5º (red stars). Two possible locations (yellow squares) of the low velocity anomaly are plotted.

So as to fit slow later phases (AB and BC) at large distances (21º~29º), triplicated raypaths at two distances (15º and 21.5º) are investigated (Fig.18). By comparing the 3-D synthetics of the "contour_g" model with the observed data, the only required anomaly is the low velocity structure on the raypath of AB and BC phases at large distances (from 21.5º to 29º), which should not interfere with other phases (including CD phase at large distances and all of the three phases at small distances). The 2D raypaths imply that there are two possible positions for this low velocity anomaly. The first one is on the landward side of subducted slabs and flatting above the 660 (36-48ºN, 110-130ºE and 640-670 km). The other one is beneath the descending slab (30 km thick).

To test the first possible location, the contour_gl1 model is designed, which adds a low-velocity anomaly (-3%) region above the 660 (36-48ºN, 110-130ºE and 640-670 km)

to the contour_g model. My simulation shows not only the later arrival times but also larger amplitudes of AB and BC phases that better match the observed waveforms at large distances (Fig.19a and 19b). On the other hand, the contour_gl2 model, superimposing a 30-km low-velocity (-3%) anomaly beneath the subducted slab on the contour_g model, was used to demonstrate the other possible location. Although still slower and higher amplitude later arrivals are required for the synthetics to match the observations in the distance range of 21º~29º, the calculation shows improvements compared with the model contour_g (Fig.19c and 19d). There is no doubt that better simulating the complex geometry and heterogeneities of the cold slab and low velocity anomalies could improve our waveform modeling results. But it would be hard to fully constrain these structures with a finite data set, and I am limited by current computational ability for 3D triplication waveform modeling. According to above raypath analysis and 3D waveform modeling results, the basic feature of the velocity perturbation model under northeast Asia is a 100km thick, 5% fast slab extending downward to ~560 km, associated with either a landward low-velocity anomaly above the 660 or a low-velocity anomaly in the sub-slab region. I now compare these results to prior studies and interpret their meaning for deep slab structure in the region.

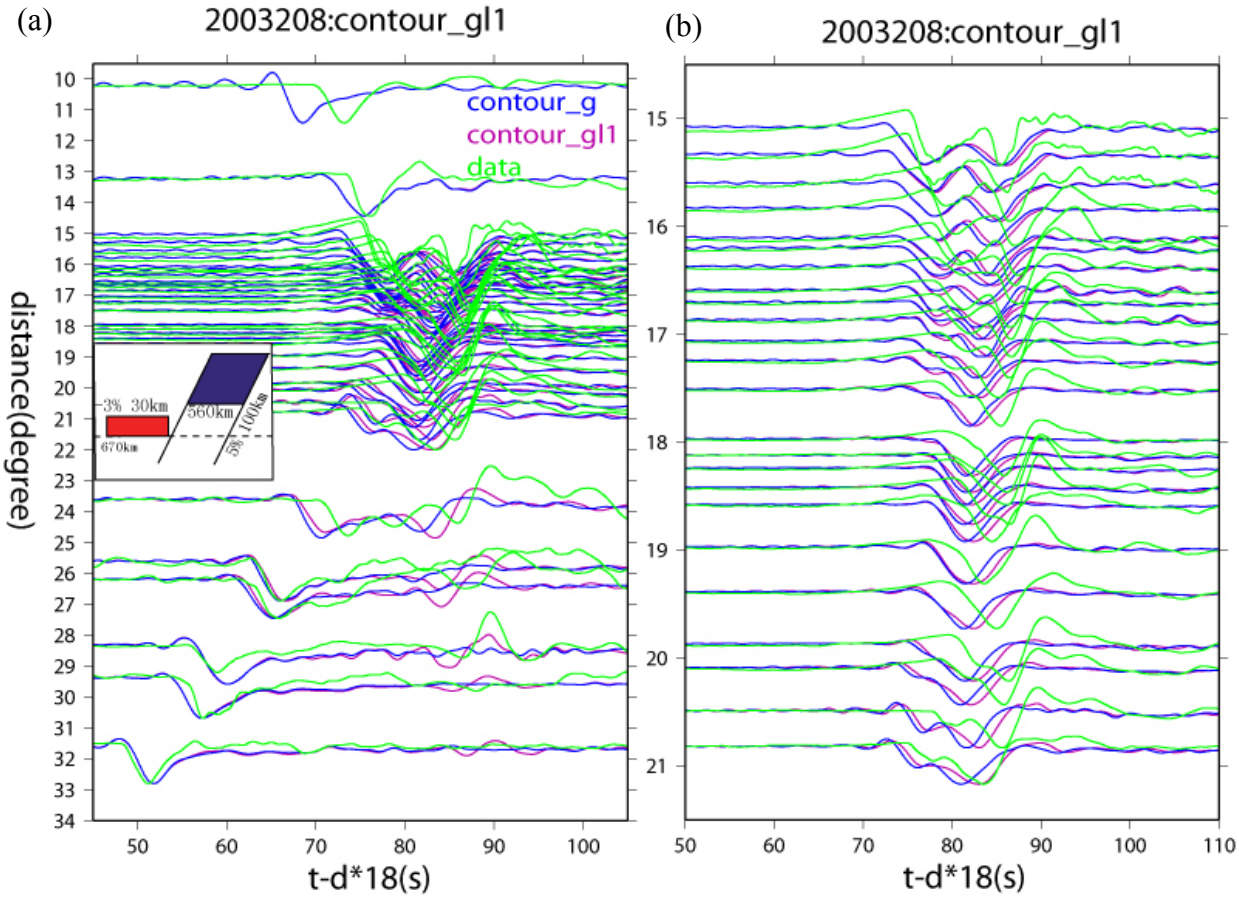

Figure 19: Comparisons of observed tangential displacements for event 2003208 (green traces) and synthetic waveforms for the model contour_g (blue traces), contour_gl1 (purple traces in a and b) and contour_gl2 (purple traces in c and d). (b) and (d) are enlarged part of (a) and (c), respectively. Schematic velocity anomalies for the model contour_gl1 and contour_gl2 are shown (small panel in a and c, respectively).

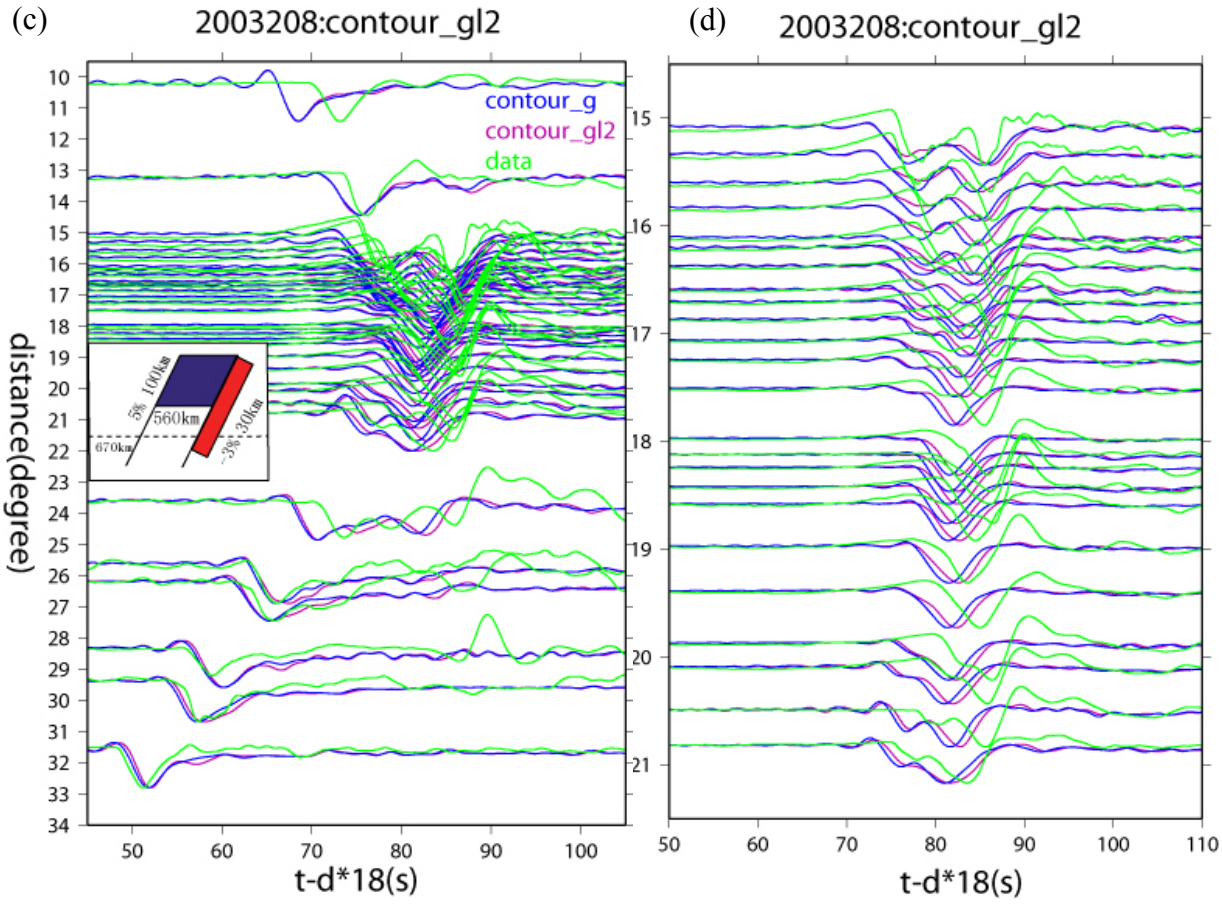

Figure 19 *(continued)*

3.2 Discussion

3.2.1 High velocity anomaly for the cold slab

Although there is a trade-off between the sign of the high-velocity slab anomaly and slab thickness in our modeling, it is reasonable to assume the thermal lithosphere thickness of 100 km, corresponding to global mean age (~100Ma) of the seafloor [*Stern*, 2002]. The +5% high velocity anomaly is consistent with regional tomography of *Zhao et al.* (1994), which has high-resolution. Their P wave tomographic image suggests the Pacific slab beneath Japan has a thickness of 80-90 km and velocity 4-6% higher than the normal mantle. However, regional tomography, limited by the poor resolution in the mantle transition zone, can not resolve how deep the high velocity anomalies of the cold slabs can extend. In this study, our waveform modeling suggests the descending slab with 5% high SH velocity subducts to at least 560 km. Around the 660, normal mantle velocity provides a better match to the observations. This result contradicts previous tomographic studies in Japan and Izu-Bonin, which image a subducted slab with 1~2% high velocity horizontally deflected above the 660 [*Fukao et al.*, 2001; *Van der hilst et al.*, 1991]. This discrepancy may be attributable to the insignificant influence of such a small perturbation on triplicated arrivals or to the poor imaging control of the 1~2% velocity anomaly in global tomography. In addition, it is difficult for one event to fully explore how the high velocity anomaly of the slab changes to normal velocity -- suddenly or gradually. In the future, if more data can be involved in the 3D triplication waveform modeling, it will be possible to constrain more precise structure for the subducted slab. Thermal conduction during the subduction process or meta-stable olivine in the mantle

transition zone might be the reason for the contrast of the velocity perturbation above 560 km and below it down to the 660-km discontinuity. That is outside the scope of this study and will require substantial future research.

3.2.2 Low velocity anomaly

3.2.2.1 Above the 660

Besides on the landward side and above the 660, there are two other possible locations for the low velocity anomaly that need to be considered. The first places the low velocity anomaly below the 660. This should only influence timing of the CD phase, not AB or BC which do not penetrate the 660. To test this, I constructed model contour_gld, which adds a 30-km thick low-velocity anomaly below the 660 (from 670 km to 700 km) in the region of 110~130ºE and 36~48ºN to model contour_g. As expected, only the amplitudes of later spikes became larger but there is no influence to their travel-times (Fig. 20a) in the model contour_gld. This is because low velocity anomaly below the 660 increases the coefficients of the reflected phase BC. But the raypaths of AB and BC phases aren't affected by this low velocity anomaly. The other possibility is a depression of the 660. Given the negative Clayperon slope of the 660, a cold slab results in a depressed 660. Because the seismic velocity of ringwoodite is lower than that of the lower mantle minerals perovskite and magniwustite, a depressed 660 appears as a region of low velocities bounded by the depressed discontinuity and its usual depth. To mimick this, I designed model contour_gd720, which moves the 660 from 670 km (the depth of the 660 in PREM) down to 720 km in model contour_g. Both 1D and 3D simulations indicate thatthe slowness of the later phase behaves opposite of our observed data. The

1D result was verified in a previous study [*Wang and Chen*, 2009]. For our 3D simulation, the later spikes go from slow at small distances to fast at large distances, compared with both the model contour_g and observations (Fig. 20b). Although I have not yet tested localized depressions of the 660, it would appear that the the opposite slowness behaviors of later phases in data and synthetics indicates a depressed 660 is an unlikely solution.

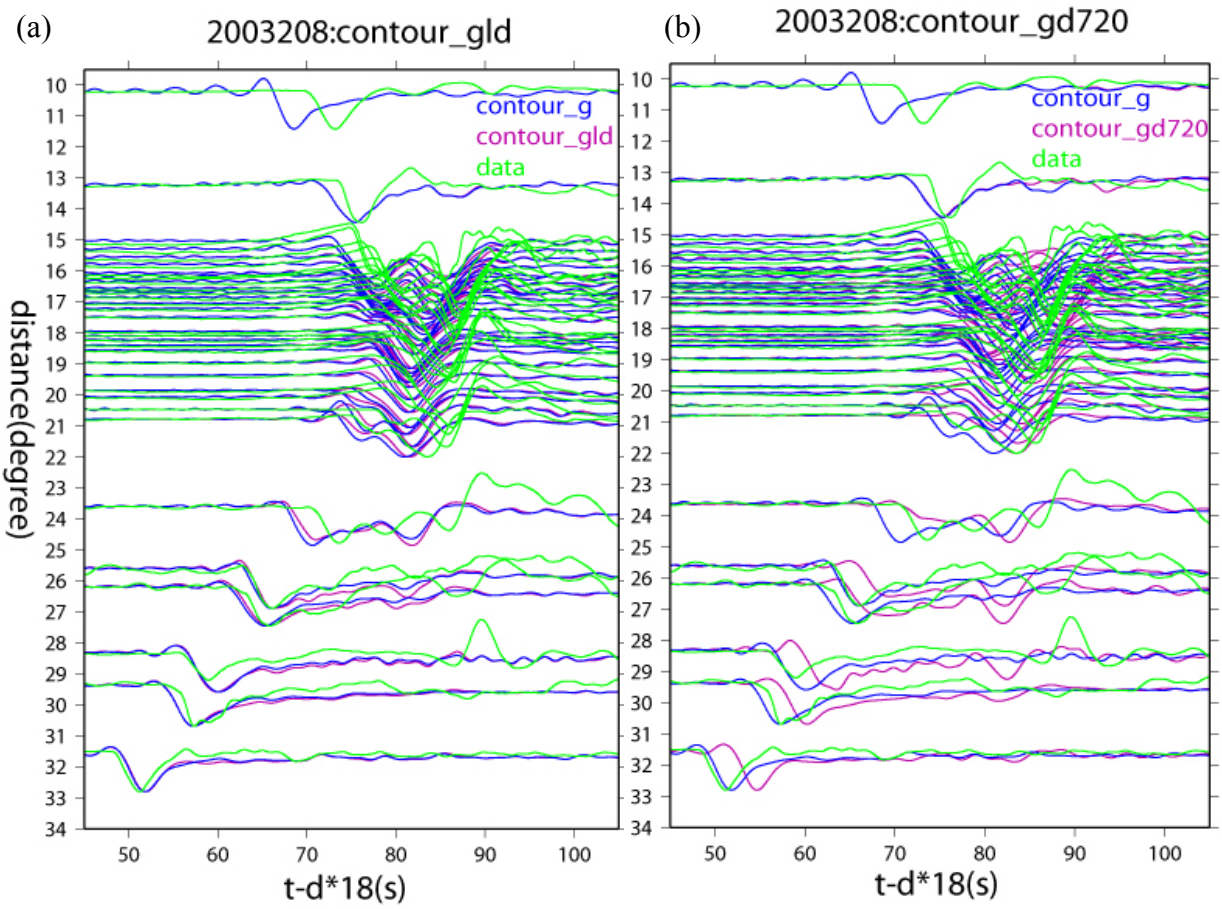

Figure 20: Comparisons of observed tangential displacements for event 2003208 (green traces) and synthetic waveforms for the model contour_g (blue traces), contour_gld (red traces in a) and contour_gd720 (red traces in b).

Beneath Eastern China, our contour_gl1 model appears to contradict previous

tomographic studies. Tomographic images show the high-velocity slab stagnantly flatten above the 660 [*Fukao et al.*, 2001; *Huang and Zhao*, 2006] or reach a depth of 800 km [*Bijwaard et al.*, 1998]. They also show high velocity anomaly for the cold slabs around the 660 with no low velocity anomaly above the 660 as our preferred model contour_gl1. Nevertheless, this low velocity anomaly above the 660 is consistent with a the receiver function study of *Ai et al.* (2008). That study identifies an uplifted 660 and thinned transition zone (~15 km) beneath the North Yellow Sea (38ºN~42ºN and 122ºE~126ºE). They interpret this small scale anomaly as either a hot upwelling from the lower mantle or small scale convection above a deeply penetrated slab. If the slab does flatten out above the 660 as tomographic images suggest, the model of a hot upwelling from the lower mantle might imply that there might be some breaks between still subducted lithosphere and the flattened slab. Complex slab geometry near the 660 might result in small scale convection above the slab. However, these two interpretations need further study. In the contour_gl1 model, the area of low-velocity anomaly contains the North Yellow Sea, though we can't constrain its borders accurately. Because the scale of the low velocity anomaly may be small as the receiver function and our study reveal, it would be difficult for tomography to image.

3.2.2.2 Beneath the slab

The transition zone is thought to be a possible water reservoir [*Bercovici and Karato*, 2003] because of high water solubility of wadsleyite and ringwoodite (2~3wt%) compared with olivine and perovskite. But electrical conductivity indicates it may be dry (0.1wt% or less) [*Yoshino et al.*, 2008]. Dehydration happens on the top side of the slab, and whether water is recycled down to the transition zone or lower mantle is still under debate. Sub-slab structure may be important in this debate. Shielded by the slab from water produced during dehydration, the sub-slab region should be closer to ambient mantle conditions than the mantle wedge. Proximity to local seismicity and strong thermal gradients offer several avenues for seismic "hygrometry", in particular the presense or absence of melt above the 410-km discontinuity, beneath the 660 and the pressure and interval width of both discontinuities. Unfortunately the sub-slab region does not lend itself well to tomographic imaging, especially the higher resolution local approaches.

Low-velocity anomalies are present under the western Pacific slabs in some tomographic images [*Honda et al.*, 2007; *Zhao et al.*, 2007]. Due to poor ray coverage below 500km depth in these studies, it is unclear whether the anomalies are real or just imaging artifacts due to the strong high-velocity slab anomalies. Some triplicated waveform modeling studies reveal low velocity anomalies under subducted slabs as well. But those previous studies were based on 1D triplication waveform modeling [*Obayashi et al.*, 2006; *Wang and Chen*, 2009].

Event 2003208 presents an opportunity to look below the slab at the base of the

transition zone. In prior 1D triplication waveform modeling of this even, a low-velocity anomaly, increasing in magnitude with depth above the 660 was proposed [*Wang and Chen*, 2009]. My 3D modeling requires no increase of velocity variation but a tilted structure which is parallel to the slab. This shape of the low-velocity anomaly is more consistent with the hot mantle entrainment model [*Honda et al.*, 2007]. The discrepancy between 1D and 3D studies could be due to misinterpretation of the lateral heterogeneity in 1D triplication waveform modeling, which I have discussed previously. Because 1D modeling shows only depth-average results, the tilted low-velocity anomaly would be canceled out or muted by the high velocity slab at shallow sub-slab depths. But, around the 660, there is negligible high-velocity for the slab based on my 3D waveform modeling. Therefore a larger low-velocity anomaly is expected in 1D modeling. Moreover, 1D triplication waveform modeling can not constrain abrupt velocity decreases. When the perturbations are local or small scale, the results of 1D method must contain some distortion, especially if the structures are inclined. Given these considerations, the inclined, discrete low-velocity anomaly obtained by 3D modeling likely is a much better depiction of true sub-slab structure. Although it is important to note that this is only one of two possible configurations for the low-velocity anomaly required by later phases in the 21 to 29 degree distance range.

I investigate three possible mechanisms of producing a low-velocity anomaly beneath the subducted slab. Based on the shape of the low velocity zone at depths around the 410 in tomographic images, numerical modeling implied a hot anomaly originally produced in the area of the Pacific superplume could be carried toward the Japanese

Islands by the horizontal flow associated with the plate movement [*Honda et al.*, 2007]. However, the results of 1D triplication waveform modeling showed no obvious reduction of the velocity variation with increasing depth, which didn't support the hot sinking scenario [*Wang and Chen*, 2009]. Instead, an upwelling plume rooted in the deep lower mantle was considered a possible reason for low velocity structure in Northern Honshu [*Obayashi et al.*, 2006] and Southern Kurile [*Wang and Chen*, 2009]. But our 3D triplication waveform modeling demonstrates that the 1D method could be affected by the geometries of wave propagation and the slab. Therefore the previous 1D preferred models [*Wang and Chen*, 2009; *Obayashi et al.*, 2006] should be considered with more than a little skepticism. If the low-velocity anomaly beneath the slabs is real as my 3D modeling suggests, the hot sinking model would be preferred because of the geometry of the anomaly (30 km thick and inclined to mirror the slab dip angle). To differentiate between these two mechanisms, more precise seismic structural control, such as topographic variations of the 660 and anomalies of P wave velocity, is needed. Thirdly, Lowman et al. (2007) found the complex configuration of downwelling features could result in warmer material below downwelling slabs. Whether this warmer material is enough to cause 3% low velocity anomaly is doubtful, but beyond the scope of this study.

3.3 Conclusions

By adopting Spectral Element Methods, we calculated full synthetic triplicated SH shear waves. In subduction zones, my parallel computations demonstrate that both the travel time and waveforms of shear waves interacting strongly with the 660-km

discontinuity were significantly affected by the geometries of wave propagation and the slab. We used depth contours to determine the geometry of the Pacific slabs and constrained 3D SH velocity structure in the mantle transition zone beneath the Southern Kurile subduction region in northeast Asia. My modeling results reveal a high velocity anomaly (+5%) for the 100-km thick cold slab extending to ~560 km depth. Normal velocity structure, or at least a much smaller perturbation (e.g. +1%) for the slab, is implied from 560 km to 670 km. To match late AB and BC branches at large distances (21º~29º), two possible locations of a low-velocity anomaly, indicated by both raypaths analysis and waveform modeling, were determined. The first places the anomaly on the landward side of the subducted slab and above the 660-km discontinuity. Within the anomaly SH velocity is reduced by 3% compared with PREM, covering the region of 110~130ºE, 36~48ºN and 640~670 km. This hot anomaly may be generated by a hot upwelling from lower mantle or small scale convection above a deeply penetrating slab. The other location is beneath the subducted slab (-3% and 30 km thick), which could be due to a hot sinking anomaly emplaced at shallower depths away from the subduction zone. Which of these two candidate locations is the cause of late arrivals and which interpretation is more reasonable are questions requiring further study.

Chapter 4, Numerical modeling

To understand what might affect the topography of the oceanward 660, I designed two suites of geodynamical models run on the massively parallel resources of MSI. The particular goal of the modeling is to demonstrate that hot anomaly originally emplaced at shallower depths can be entrained by subducting slabs and reach depths sufficient to influence the 660. A second goal is to see whether this hot entrained model can explain observations from chapter 2, namely that steeper slab subduction dip corresponds to locally higher temperatures (and shallower 660) in the sub-slab region of the western Pacific.

4.1 Method and Initial and Boundary conditions

I implemented the finite element code (CITCOMS) from CIG (Computational Infrastructure for Geodynamics) on the "Itasca" resource of MSI [*Zhong et al.*, 2000; *Tan et al.*, 2006]. Primed parameters in the following paragraphs, such as temperature, viscosity and pressure, are normalized and non-dimensional. Three equations for conservation of mass, momentum and energy govern the convection. In the incompressible case, they are solved by the Uzawa algorithm [*Cahouet et al.*, 1988] and iteration method (conjugate gradient).

To compare the influence of the slab dip angle on hot entrained anomalies, two models with different initial dips of subduction were created. In the subducting direction, grid spacing in the subduction zone is denser than other regions. In the trench direction, grid spacing is uniform. In the vertical dimension, grids are denser near the surface.

Initially, the normalized temperature of the cold lithosphere (~95.6 km thick) is 0, while it is 1.4 for the hot anomaly (~127.4 km thick) beneath the cold slab. Other regions are set to 1 (Fig. 21). In each calculation step, the temperature for the lithosphere (<100 km) is updated and is set to 0 (subduction is always right vergent in my models). To keep the temperature at zero for the lithosphere all the time steps, we added "temp=0.0;" below "temp = (E->sphere.ro-r1) *0.5 /sqrt(E->age_t[nodeg]);" in "Lith_age.c". Since only subdction process need to be focused in the whole mantle convection circle, the updated lithosphere can short the required total width of our models and save the resource. Temperature-dependent viscosity is computed by: $\eta = \eta_0 \times \exp(\frac{E_\eta}{T^* + T_\eta} - \frac{E_\eta}{1 + T_\eta})$, where T*=min(max(T,0),1) and all other parameters are equal to 1 except the pre-exponent factor η_0 of layered viscosity structure. For initial viscosity, two layers are assigned to the left-side oceanic slab. The pre-exponent factor is 0.03 for the upper layer (12.7 km) and 100 for the rest of the slab (Fig.22), representing the weak basalt layer and rigid pyrolite lithosphere layer, respectively. Presence of the low viscosity layer on the top of subducting lithosphere enhances the subduction process. The right-hand side of the domain models continental lithosphere, and I set the pre-exponent factor to 100 from the surface to 95.6 km. The pre-exponent factor is 1 in the sub-lithospheric upper mantle and 2 in the lower mantle. Constant velocity boundary conditions are applied to the surface. The right-side continental lithosphere is fixed at 0 cm/yr. The horizontal movement of the oceanic slab is set to 10 cm/year towards the trench.

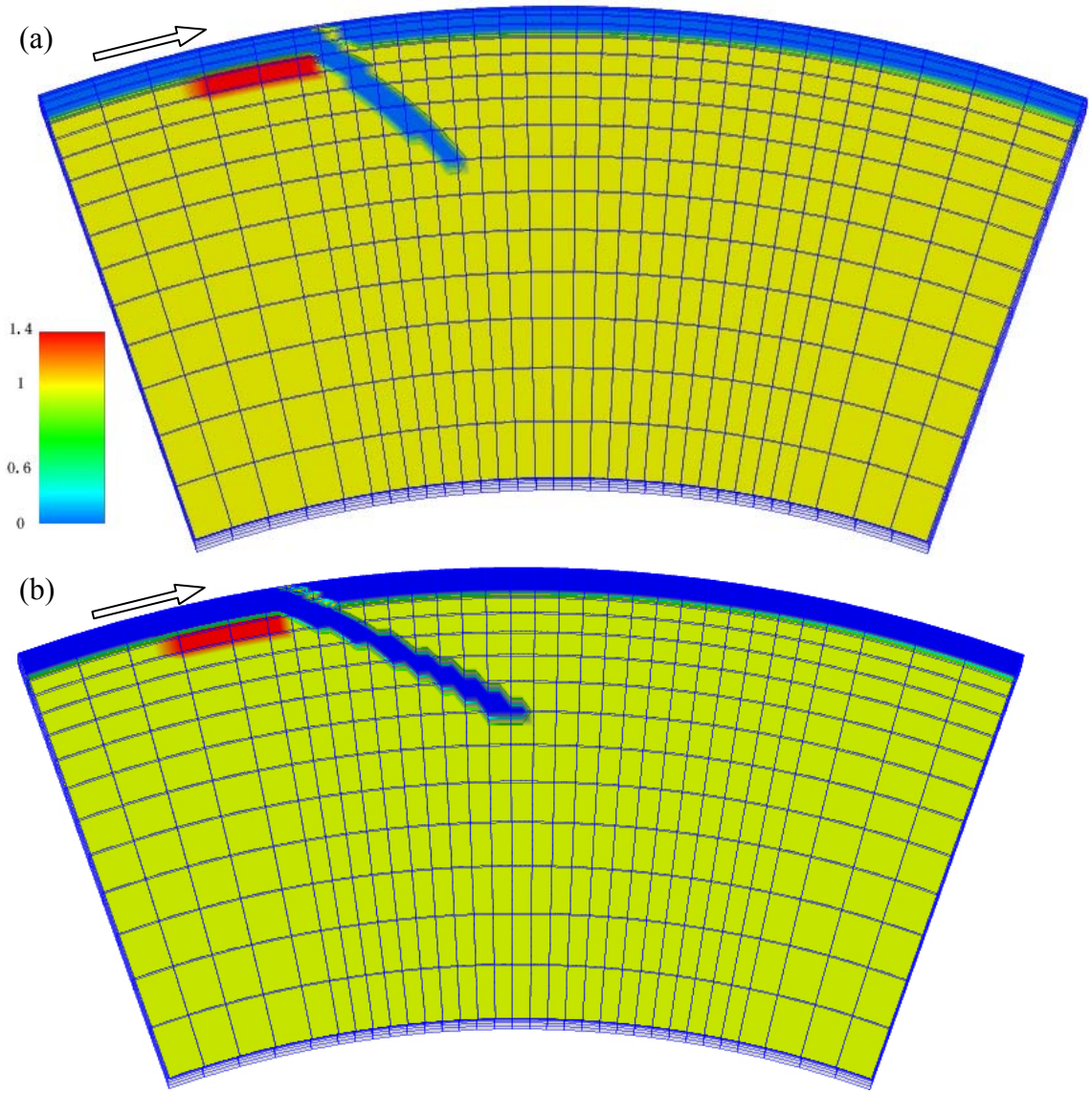

Figure 21: Initial conditions for the 45^{o} (a) and 30^{o} (b) slabs (blue). Hot anomaly beneath cold lithosphere (red) and 10cm/year velocity for the left-side oceanic plate (arrow) are drawn. For simplicity, grids are reduced to half and connected by blue lines.

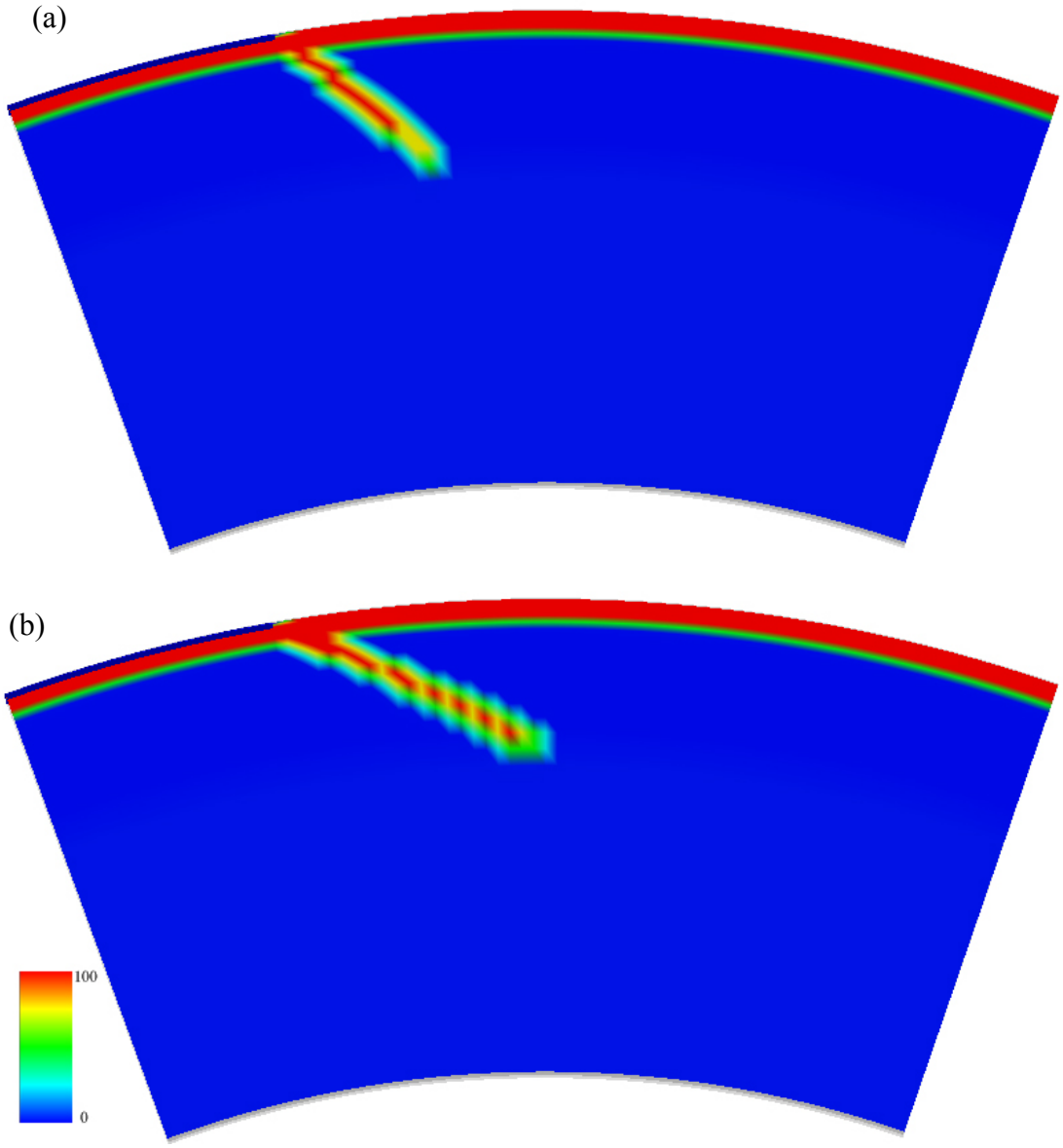

Figure 22: The initial pre-exponent factor η_0 of layered viscosity for the 45° (a) and 30° (b) slabs (red). The weak basalt layer (12.7 km, blue) is on the top of left-side oceanic lithosphere.

4.2 Results and discussion

Although these models are simple, the outcome demonstrates the hot entrained mantle scenario is a possible mechanism to explain the seismic observations of Chapters 2 and 3. Subducted oceanic lithosphere, due to high sub-slab viscosity, can drag the underlying hot anomaly into the transition zone and to the 660. Given equal rates of subduction, the hot anomaly requires less time to get to the 660 discontinuity for a more steeply dipping slab. This leads to a decreasing convection time and thus higher temperature. My dynamical modeling result is consistent with the kinematic study of *Honda et al.* (2007). Their result indicates the entrained hot anomaly influences the 410 more as the dip of the slab increases. Here, my calculations suggest that the dip angle of slabs affects not only the appearance of the hot anomaly but also the temperature at the oceanward 660 (Fig. 23 and 24). At step 300 (17.3Myr), the temperature in the mantle transition zone is 12% higher than normal mantle for the 45° slab (Fig. 24a) while it is only 2% higher for the 30° slab (Fig. 24b).

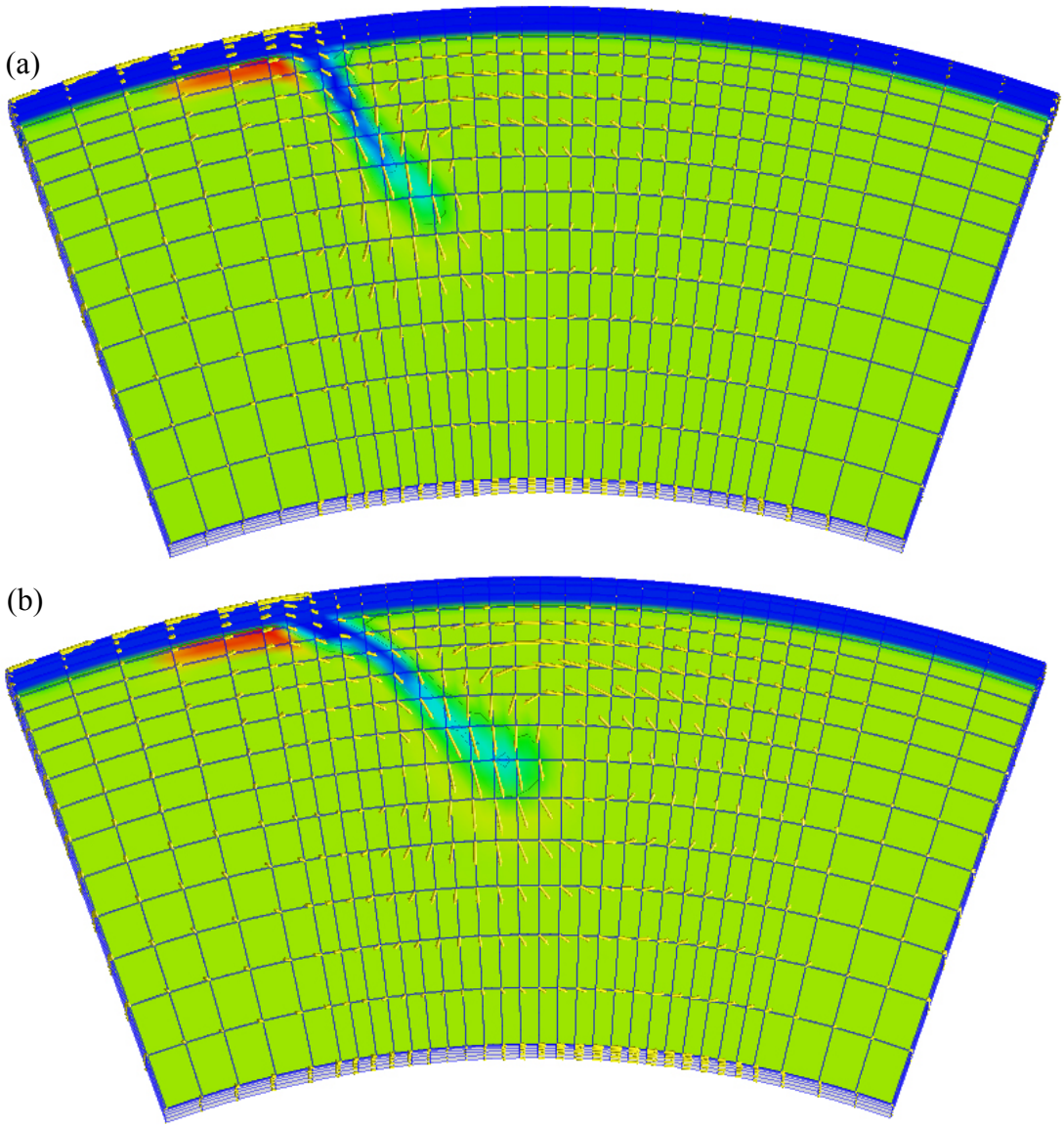

Figure 23: Snapshots at step 40 (2.257Myr) for both 45° (a) and 30° (b) slabs (blue). Yellow arrows are presenting the dynamic velocity.

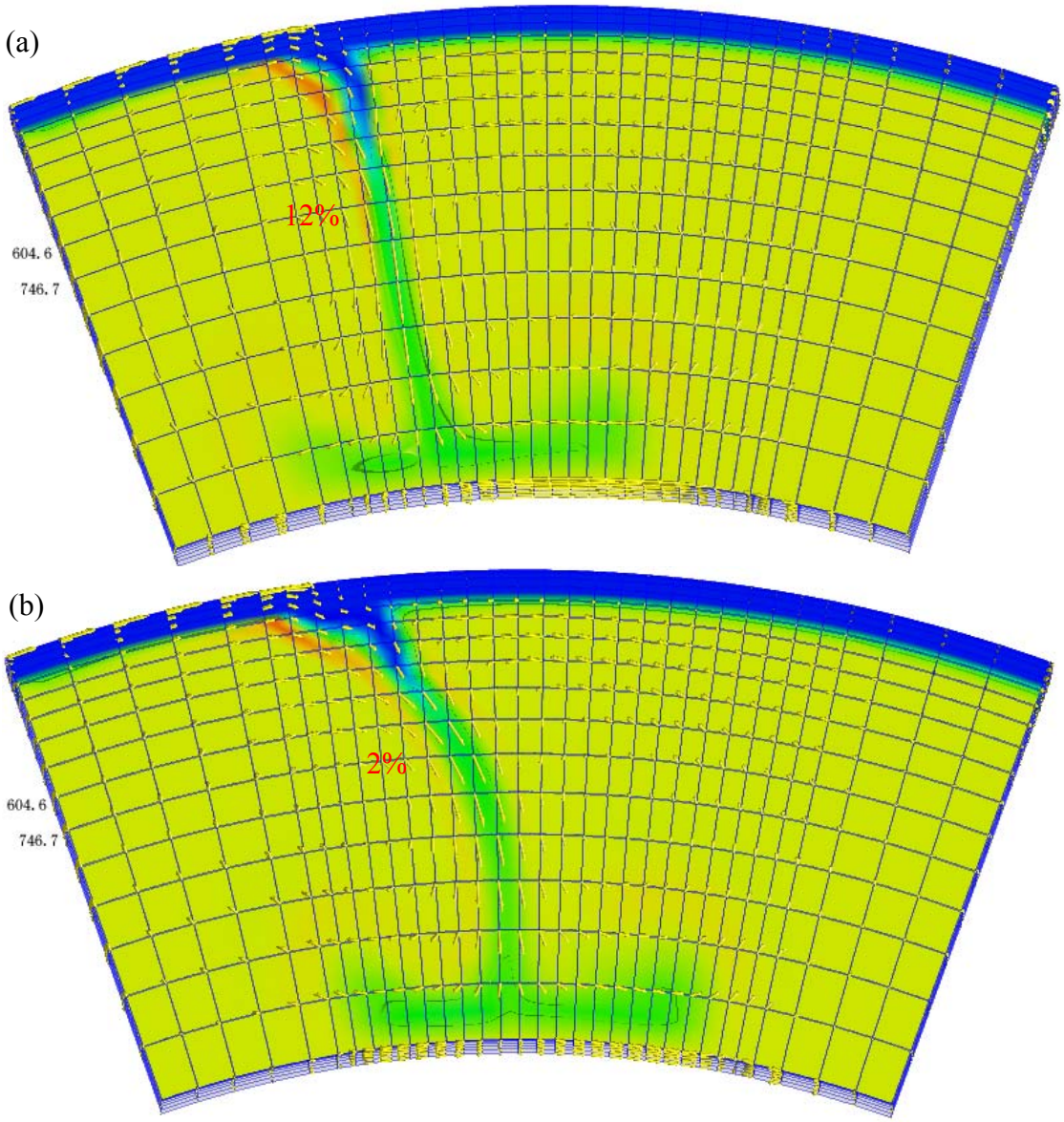

Figure 24: Snapshots at step 300 (17.3Myr) for both 45° (a) and 30° (b) slabs (blue). Temperatures around the 660 beneath subducted slabs are 12% (a) and 2% (b) higher than normal mantle, respectively.

Our simple numerical modeling confirms that a hot entrained mantle anomaly can reach the 660, producing a local uplift in the sub-slab region, similar to the uplifted 660 documented in Chapter 2 and the low SH velocity anomaly beneath subducting slabs suggested in Chapter 3. Slab dip matters and follows the trend observed in Chapter 2, namely that the 660 is uplifted more beneath steeply dipping slabs.

Chapter 5, Conclusions

To explore seismic structure near the 660, S-to-P converted phases and 3D triplicated waveform mdeling were employed to unveil the topography of the sub-slab 660 in the Western Pacific and SH anomalies in the mantle transition zone, respectively. Our study demonstrates that it is feasible to investigate the 660 beneath subducting slabs by stacking S660P over a large distance range. The results reveal that the topography of the sub-slab 660 varies considerably from region to region in the Western Pacific. On the one hand, in the northwestern Pacific, beneath the Philippine Sea and Southern Kurile Islands, the average depth of this discontinuity is elevated ~10 km and ~6.5 km, respectively. Meanwhile, it is normal beneath the Sea of Japan where a sub-horizontally flattened slab above the 660-km discontinuity previously has been found. On the other hand, it is ~11.5 km and ~6.4 km shallower beneath subduction zones of the Marianas and Tonga Islands, respectively. The topographic variation suggests that the 660-km discontinuity beneath subducting slabs shallows as the dip of the slab increases.

Using the spectral element method, the results of 3D triplication waveform modeling imply that the waveforms of shear waves interacting strongly with the 660-km discontinuity are significantly affected by the geometries of wave propagation and the slab. Moreover, beneath the Southern Kurile, our best fitting model indicates the high-velocity slab (+5% anomaly and ~100km thick) might subduct, at least, to 560 km while no obvious high-velocity anomaly of the slab is observed around the 660. To match late AB and BC branches at large distances, two alternative locations of low-velocity anomaly (-3% and ~30km thick) are possible. The first is beneath the subducted slab,

which might be due to a hot entrained anomaly emplaced at shallower depths away from the subduction zone. The other location is the landward side of the subducted slab and above the 660-km discontinuity. We suggest this hot anomaly could be generated by a hot upwelling from the lower mantle or small scale convection above a deeply penetrating slab.

Lastly, the scenario of a hot entrained anomaly is tested by geodynamical modeling. My calculations suggest that a hot entrained anomaly could explain the seismic observations outlined above. The hot anomaly beneath subducting slabs is effectively dragged by the slab into the transition zone. It can reach and hence uplift the 660. Simultaneously, it is hotter in the transition zone when the dip angle of the slab is greater. The geometry of this high temperature region beneath the slab is consistent with the first possible location of the low-velocity anomaly.

Bibliography:

Akaogi, M., E. Ito, and A. Navrotsky (1989), Olivine-Modified Spinel-Spinel Transitions in the System Mg2sio4-Fe2sio4 - Calorimetric Measurements, Thermochemical Calculation, and Geophysical Application, *Journal of Geophysical Research-Solid Earth and Planets, 94(B11)*, 15671-15685.

Ai, Y. S., T. Y. Zheng, W. W. Xu, Y. M. He, and D. Dong (2003), A complex 660 km discontinuity beneath northeast China, *Earth and Planetary Science Letters, 212*(1-2), 63-71.

Ai, Y., T. Zheng, W. Xu, and Q. Li (2008), Small scale hot upwelling near the North Yellow Sea of eastern China, *Geophys. Res. Lett., 35, L20305*, doi:10.1029/2008GL035269.

Andrews, J., and A. Deuss (2008), Detailed nature of the 660 km region of the mantle from global receiver function data, *J. Geophys. Res., 113, B06304*, doi:10.1029/2007JB005111.

Benz, H. M., and J. E. Vidale (1993), Sharpness of Upper-Mantle Discontinuities Determined from High-Frequency Reflections, *Nature, 365(6442)*, 147-150.

Bercovici, D., and S. Karato (2003), Whole-mantle convection and the transition-zone water filter, *Nature, 425(6953)*, 39-44.

Bijwaard, H., W. Spakman, and E. R. Engdahl (1998), Closing the gap between regional and global travel time tomography, *Journal of Geophysical Research-Solid Earth, 103(B12)*, 30055-30078.

Bina, C. R., and G. Helffrich (1994), Phase-Transition Clapeyron Slopes and Transition

Zone Seismic Discontinuity Topography, *Journal of Geophysical Research-Solid Earth, 99(B8)*, 15853-15860.

Cahouet, J., and J.-P. Chabard (1988), Some fast 3D finite element solvers for the generalized Stokes problem, *Int. J. Numer. Methods. Fluids, 8*, 869-895

Chen, J. H., D. J. Weidner, and M. T. Vaughan (2002), The strength of Mg(0.9)Fe(0.1)SiO(3) perovskite at high pressure and temperature, *Nature, 419(6909)*, 824-826.

Chen, W. R., and M. R. Brudzinski (2001), Evidence for a large-scale remnant of subducted lithosphere beneath Fiji, *Science, 292(5526)*, 2475-2479.

Di Leo, J. F., J. Wookey, J. O. S. Hammond, J. M. Kendall, S. Kaneshima, H. Inoue, T. Yamashina, and P. Harjadi (2012), Deformation and mantle flow beneath the Sangihe subduction zone from seismic anisotropy, *Physics of the Earth and Planetary Interiors, 194*, 38-54.

Fei, Y., J. Van Orman, J. Li, W. van Westrenen, C. Sanloup, W. Minarik, K. Hirose, T. Komabayashi, M. Walter, and K. Funakoshi (2004), Experimentally determined postspinel transformation boundary in Mg2SiO4 using MgO as an internal pressure standard and its geophysical implications, *Journal of Geophysical Research-Solid Earth, 109(B2)*, doi:10.1029/2003JB002562.

Flanagan, M. P., and P. M. Shearer (1998), Global mapping of topography on transition zone velocity discontinuities by stacking SS precursors, *Journal of Geophysical Research-Solid Earth, 103(B2)*, 2673-2692

Foley, B. J., and M. D. Long (2011), Upper and mid-mantle anisotropy beneath the

Tonga slab, *Geophys. Res. Lett., 38, L02303*, doi:10.1029/2010GL046021.

Frost, D. J., and Y. W. Fei (1998), Stability of phase D at high pressure and high temperature, *Journal of Geophysical Research-Solid Earth, 103(B4)*, 7463-7474.

Fukao, Y., S. Widiyantoro, and M. Obayashi (2001), Stagnant slabs in the upper and lower mantle transition region, *Reviews of Geophysics, 39(3)*, 291-323.

Gu, Y., A. M. Dziewonski, and C. B. Agee (1998), Global de-correlation of the topography of transition zone discontinuities, *Earth and Planetary Science Letters, 157(1-2)*, 57-67.

Gu, Y. J., and A. M. Dziewonski, Global variability of transition zone thickness, *J. Geophys. Res., 107(B7)*, doi:10.1029/2001JB000489, 2002.

Gudmundsson, O., and M. Sambridge (1998), A regionalized upper mantle (RUM) seismic model, *Journal of Geophysical Research-Solid Earth, 103(B4)*, 7121-7136.

Hirschmann, M. M. (2006), Water, melting, and the deep Earth H2O cycle, *Annual Review of Earth and Planetary Sciences, 34*, 629-653.

Honda, S., M. Morishige, and Y. Orihashi (2007), Sinking hot anomaly trapped at the 410 km discontinuity near the Honshu subduction zone, Japan, *Earth and Planetary Science Letters, 261(3-4)*, 565-577.

Huang, J., and D. Zhao (2006), High-resolution mantle tomography of China and surrrounding regions, *JOURNAL OF GEOPHYSICAL RESEARCH, 111(B09305)*, doi:10.1029/2005JB004066.

Huang, X. G., Y. S. Xu, and S. I. Karato (2005), Water content in the transition zone from electrical conductivity of wadsleyite and ringwoodite, *Nature, 434(7034)*, 746-

749.

Hutko, A. R., T. Lay, J. Revenaugh, and E. J. Garnero (2008), Anticorrelated seismic velocity anomalies from post-perovskite in the lowermost mantle, *Science, 320(5879)*, 1070-1074.

Inoue, T., H. Yurimoto, and Y. Kudoh (1995), Hydrous Modified Spinel, Mg1.75sih0.5o4 - a New Water Reservoir in the Mantle Transition Region, *Geophysical Research Letters, 22(2)*, 117-120.

Inoue, T., D. J. Weidner, P. A. Northrup, and J. B. Parise (1998), Elastic properties of hydrous ringwoodite (gamma-phase) in Mg2SiO4, *Earth and Planetary Science Letters, 160(1-2),* 107-113.

Jacobsen, S. D., J. R. Smyth, H. Spetzler, C. M. Holl, and D. J. Frost (2004), Sound velocities and elastic constants of iron-bearing hydrous ringwoodite, *Physics of the Earth and Planetary Interiors, 143-44*, 47-56.

Kaneshima, S., and G. Helffrich (1999), Dipping low-velocity layer in the mid-lower mantle: Evidence for geochemical heterogeneity, *Science, 283(5409)*, 1888-1891.

Karato, S. (1993), Importance of Anelasticity in the Interpretation of Seismic Tomography, Geophysical Research Letters, *20(15)*, 1623-1626.

Karato, S. (1995), Effects of Water on Seismic-Wave Velocities in the Upper-Mantle, *Proceedings of the Japan Academy Series B-Physical and Biological Sciences, 71(2)*, 61-66.

Karato, S. (2011), Water distribution across the mantle transition zone and its implications for global material circulation, *Earth and Planetary Science Letters,*

301(3-4), 413-423.

Kawakatsu, H., and S. Watada (2007), Seismic evidence for deep-water transportation in the mantle, *Science, 316(5830)*, 1468-1471.

Kennett, B. L. N., and E. R. Engdahl (1991), Traveltimes for Global Earthquake Location and Phase Identification, *Geophysical Journal International, 105(2)*, 429-465.

Kohlstedt, D. L., H. Keppler, and D. C. Rubie (1996), Solubility of water in the alpha, beta and gamma phases of (Mg,Fe)(2)SiO4, *Contributions to Mineralogy and Petrology, 123(4)*, 345-357.

Komatitsch, D., J. Ritsema, and J. Tromp (2002), The spectral-element method, beowulf computing, and global seismology, *Science, 298(5599)*, 1737-1742.

Komatitsch, D., G. Erlebacher, D. Goddeke, and D. Michea (2010), High-order finite-element seismic wave propagation modeling with MPI on a large GPU cluster, *Journal of Computational Physics, 229(20)*, 7692-7714.

Kustowski, B., G. Ekström, and A. M. Dziewoński (2008), Anisotropic shear-wave velocity structure of the Earth's mantle: A global model, *J. Geophys. Res., 113, B06306*, doi:10.1029/2007JB005169.

Lawrence, J. F., and P. M. Shearer (2006), A global study of transition zone thickness using receiver functions, J. *Geophys. Res., 111, B06307,* doi:10.1029/2005JB003973.

Lebedev, S., S. Chevrot, and R. D. van der Hilst (2003), Correlation between the shear-speed structure and thickness of the mantle transition zone, *Physics of the Earth and Planetary Interiors, 136(1-2)*, 25-40.

Li, J., Q.-F. Chen, E. Vanacore, and F. Niu (2008), Topography of the 660-km

discontinuity beneath northeast China: Implications for a retrograde motion of the subducting Pacific slab, *Geophys. Res. Lett., 35, L01302*, doi:10.1029/2007GL031658.

Li, X., S. V. Sobolev, R. Kind, X. Yuan, and C. Estabrook (2000), A detailed receiver function image of the upper mantle discontinuities in the Japan subduction zone, *Earth and Planetary Science Letters, 183(3-4)*, 527-541.

Li, X. Q., and X. H. Yuan (2003), Receiver functions in northeast China - implications for slab penetration into the lower mantle in northwest Pacific subduction zone, *Earth and Planetary Science Letters, 216(4)*, 679-691.

Long, M. D., and P. G. Silver (2008), The subduction zone flow field from seismic anisotropy: A global view, *Science, 319(5861)*, 315-318.

Lowman, J. P., L. T. Pinero-Feliciangeli, J.-M. Kendall, and M. H. Shahnas (2007), Influence of convergent plate boundaries on upper mantle flow and implications for seismic anisotropy, *Geochem. Geophys. Geosyst., 8, Q08007*, doi:10.1029/2007GC001627.

Mcfadden, P. L., B. J. Drummond, and S. Kravis (1986), The Nth-Root Stack - Theory, Applications, and Examples, *Geophysics, 51(10)*, 1879-1892.

Meier, U., J. Trampert, and A. Curtis (2009), Global variations of temperature and water content in the mantle transition zone from higher mode surface waves, *Earth and Planetary Science Letters, 282(1-4)*, 91-101.

Miller, M. S., and B. L. N. Kennett (2006), Evolution of mantle structure beneath the northwest Pacific: Evidence from seismic tomography and paleogeographic

reconstructions - art. no. TC4002, *Tectonics, 25(4)*, C4002-C4002.

Muller, G. (1985), The Reflectivity Method - a Tutorial, *Journal of Geophysics-Zeitschrift Fur Geophysik, 58(1-3)*, 153-174.

Niu, F. L., and H. Kawakatsu (1995), Direct Evidence for the Undulation of the 660-Km Discontinuity beneath Tonga - Comparison of Japan and California Array Data, *Geophysical Research Letters, 22(5)*, 531-534.

Niu, F. L., and H. Kawakatsu (1998), Determination of the absolute depths of the mantle transition zone discontinuities beneath China: Effect of stagnant slabs on transition zone discontinuities, *Earth Planets and Space, 50(11-12)*, 965-975.

Nolet, G., S. P. Grand, and B. L. N. Kennett (1994), Seismic Heterogeneity in the Upper-Mantle, *Journal of Geophysical Research-Solid Earth, 99(B12)*, 23753-23766.

Obayashi, M., H. Sugioka, J. Yoshimitsu, and Y. Fukao (2006), High temperature anomalies oceanward of subducting slabs at the 410-km discontinuity, *Earth and Planetary Science Letters, 243(1-2)*, 149-158.

Ohtani, E., H. Mizobata, and H. Yurimoto (2000), Stability of dense hydrous magnesium silicate phases in the systems Mg2SiO4-H2O and MgSiO3-H2O at pressures up to 27 GPa, *Physics and Chemistry of Minerals, 27(8)*, 533-544.

Ohtani, E., K. Litasov, T. Hosoya, T. Kubo, and T. Kondo (2004), Water transport into the deep mantle and formation of a hydrous transition zone, *Physics of the Earth and Planetary Interiors, 143*, 255-269.

Ohtani, E., and T. Sakai (2008), Recent advances in the study of mantle phase transitions, *Physics of the Earth and Planetary Interiors, 170(3-4)*, 240-247.

Revenaugh, J., and T. H. Jordan (1991), Mantle Layering from Scs Reverberations .2. The Transition Zone, *Journal of Geophysical Research-Solid Earth, 96(B12)*, 19763-19780.

Revenaugh, J., and S. A. Sipkin (1994), Seismic Evidence for Silicate Melt Atop the 410 Km Mantle Discontinuity, *Nature, 369(6480)*, 474-476.

Ringwood, A. E. (1991), Phase-Transformations and Their Bearing on the Constitution and Dynamics of the Mantle, *Geochimica Et Cosmochimica Acta, 55(8)*, 2083-2110.

Ritsema, J., A. Deuss, H. J. van Heijst, and J. H. Woodhouse (2011), S40RTS: a degree-40 shear-velocity model for the mantle from new Rayleigh wave dispersion, teleseismic traveltime and normal-mode splitting function measurements, *Geophysical Journal International, 184(3)*, 1223-1236.

Rost, S., and C. Thomas, Array seismology: Methods and applications, *Rev. Geophys., 40 (3), 1008*, doi:10.1029/2000RG0001002002.

Ryberg, T., F. Wenzel, A. V. Egorkin, and L. Solodilov (1998), Properties of the mantle transition zone in northern Eurasia, *Journal of Geophysical Research-Solid Earth, 103(B1)*, 811-822.

Schmerr, N., and E. J. Garnero (2007), Upper mantle discontinuity topography from thermal and chemical heterogeneity, *Science, 318(5850)*, 623-626.

Shearer, P. M. (1991a), Constraints on Upper Mantle Discontinuities from Observations of Long-Period Reflected and Converted Phases, *Journal of Geophysical Research-Solid Earth, 96(B11)*, 18147-18182.

Shearer, P. M. (1991b), Imaging Global Body Wave Phases by Stacking Long-Period

Seismograms, *Journal of Geophysical Research-Solid Earth, 96(B12)*, 20353-20364.

Sinogeikin, S. V., J. D. Bass, and T. Katsura (2003), Single-crystal elasticity of r ingwoodite to high pressures and high temperatures: implications for 520 km seismic discontinuity, *Physics of the Earth and Planetary Interiors, 136(1-2)*, 41-66.

Smyth, J. R., C. M. Holl, D. J. Frost, and S. D. Jacobsen (2004), High pressure crystal chemistry of hydrous ringwoodite and water in the Earth's interior, *Physics of the Earth and Planetary Interiors, 143-44*, 271-278.

Song, T. R. A., D. V. Helmberger, and S. P. Grand (2004), Low-velocity zone atop the 410-km seismic discontinuity in the northwestern United States, *Nature, 427(6974)*, 530-533.

Stern, R. J. (2002), Subduction zones, *Rev. Geophys., 40 (4), 1012,* doi:10.1029/2001RG000108.

Tan, E., E. Choi, P. Thoutireddy, M. Gurnis, and M. Aivazis (2006), GeoFramework: Coupling multiple models of mantle convection within a computational framework, *Geochem., Geophys., Geosyst. 7, Q06001*, doi:10.1029/2005GC001155

Tajima, F., and S. P. Grand (1995), Evidence of High-Velocity Anomalies in the Transition Zone Associated with Southern Kurile Subduction Zone, G*eophysical Research Letters, 22(23)*, 3139-3142.

Tajima, F., Y. Fukao, M. Obayashi, and T. Sakurai (1998), Evaluation of slab images in the northwestern Pacific, *Earth Planets and Space, 50(11-12)*, 953-964.

Tajima, F., and S. P. Grand (1998), Variation of transition zone high-velocity anomalies and depression of 660 km discontinuity associated with subduction zones from the

southern Kuriles to Izu-Bonin and Ryukyu, *Journal of Geophysical Research-Solid Earth, 103(B7)*, 15015-15036.

Thirot, J. L., J. P. Montagner, and L. Vinnik (1998), Upper-mantle seismic discontinuities in a subduction zone (Japan) investigated from P to S converted waves, *Physics of the Earth and Planetary Interiors, 108(1)*, 61-80.

Tibi, R., D. A. Wiens, H. Shiobara, H. Sugioka, and X. Yuan (2007), Double seismic discontinuities at the base of the mantle transition zone near the Mariana slab, *Geophys. Res. Lett., 34, L16316*, doi:10.1029/2007GL030527.

Tonegawa, T., K. Hirahara, T. Shibutani, H. Iwamori, H. Kanamori, and K. Shiomi (2008), Water flow to the mantle transition zone inferred from a receiver function image of the Pacific slab, *Earth and Planetary Science Letters, 274(3-4)*, 346-354.

Tono, Y., T. Kunugi, Y. Fukao, S. Tsuboi, K. Kanjo, and K. Kasahara (2005), Mapping of the 410- and 660-km discontinuities beneath the Japanese islands, *J. Geophys. Res., 110, B03307*, doi:10.1029/2004JB003266.

Vacher, P., A. Mocquet, and C. Sotin (1998), Computation of seismic profiles from mineral physics: the importance of the non-olivine components for explaining the 660 km depth discontinuity, *Physics of the Earth and Planetary Interiors, 106(3-4)*, 275-298.

Van der Meijde, M., F. Marone, D. Giardini, and S. van der Lee (2003), Seismic evidence for water deep in earth's upper mantle, *Science, 300(5625)*, 1556-1558.

Van der hilst, R., R. Engdahl, W. Spakman, and G. Nolet (1991), Tomographic Imaging of Subducted Lithosphere Below Northwest Pacific Island Arcs, *Nature, 353(6339)*,

37-43.

Wang, B., and F. Niu (2010), A broad 660 km discontinuity beneath northeast China revealed by dense regional seismic networks in China, *J. Geophys. Res., 115, B06308*, doi:10.1029/2009JB006608.

Wang, R. J. (1999), A simple orthonormalization method for stable and efficient computation of Green's functions, *Bulletin of the Seismological Society of America, 89(3)*, 733-741.

Wang, T., and L. Chen (2009), Distinct velocity variations around the base of the upper mantle beneath northeast Asia, *Physics of the Earth and Planetary Interiors, 172(3-4)*, 241-256.

Wang, Y., L. X. Wen, and D. Weidner (2008), Upper mantle SH- and P-velocity structures and compositional models beneath southern Africa, *Earth and Planetary Science Letters, 267(3-4)*, 596-608.

Weidner, D. J., and Y. B. Wang (1998), Chemical- and Clapeyron-induced buoyancy at the 660 km discontinuity, *Journal of Geophysical Research-Solid Earth, 103(B4)*, 7431-7441.

Weidner, D. J., and Y. Wang (2000), Phase transformations: Implications for mantle structure, in Earth's Deep Interior:Mineral Physics and Tomography From the Atomic to the Global Scale, *Geophys. Monogr. Ser.,, 117*(edited by S.-I. Karato, A. M. Forte, R. C. Liebermann, G. Masters,and L. Stixrude, AGU, Washington, D. C.), 215-235.

Williams, Q., and R. J. Hemley (2001), Hydrogen in the deep earth, *Annual Review of*

Earth and Planetary Sciences, 29, 365-418.

Ye, L. L., J. Li, T. L. Tseng, and Z. X. Yao (2011), A stagnant slab in a water-bearing mantle transition zone beneath northeast China: implications from regional SH waveform modelling, *Geophysical Journal International, 186(2)*, 706-710.

Yoshino, T., G. Manthilake, T. Matsuzaki, and T. Katsura (2008), Dry mantle transition zone inferred from the conductivity of wadsleyite and ringwoodite, *Nature, 451(7176)*, 326-329.

Zang, S.-X., Y.-Z. Zhou, J.-Y. Ning, and R.-Q. Wei (2006), Multiple discontinuities near 660 km beneath Tonga area, *Geophys. Res. Lett., 33, L20312*, doi:10.1029/2006GL027262.

Zhao, D. P., A. Hasegawa, and H. Kanamori (1994), Deep-Structure of Japan Subduction Zone as Derived from Local, Regional, and Teleseismic Events, *Journal of Geophysical Research-Solid Earth, 99(B11)*, 22313-22329.

Zhao, D. P., K. L. Wang, G. C. Rogers, and S. M. Peacock (2001), Tomographic image of low P velocity anomalies above slab in northern Cascadia subduction zone, *Earth Planets and Space, 53(4)*, 285-293.

Zhao, D. P., S. Maruyama, and S. Omori (2007), Mantle dynamics of Western Pacific and East Asia: Insight from seismic tomography and mineral physics, *Gondwana Research, 11(1-2)*, 120-131.

Zhong, S., M.T. Zuber, L.N. Moresi, and M. Gurnis (2000), The role of temperature-dependent viscosity and surface plates in spherical shell models of mantle convection. *J. Geophys. Res., 105*, 11,063-11,082

Zheng, Y. C., T. Lay, M. P. Flanagan, and Q. Williams (2007), Pervasive seismic wave reflectivity and metasomatism of the Tonga mantle wedge, *Science, 316(5826)*, 855-859.

Zielhuis, A., and G. Nolet (1994), Shear-Wave Velocity Variations in the Upper-Mantle beneath Central-Europe, *Geophysical Journal International, 117(3)*, 695-715.

Appendix A

To decrease the searching time for certain point, regular grid structure was used. A bug in model_ppm.f90 was fixed (line 484~486). We changed the code from

“

```
index=int(                                                    (depth-
PPM_V%mindepth)/PPM_V%ddepth )*num_lonperdepth*num_latperlon  &
 + int( (lon-PPM_V%minlon)/PPM_V%dlon )*num_latperlon &
 + int( (lat-PPM_V%minlat)/PPM_V%dlat ) + 1
```

”

to

“

```
index=int((depth-
PPM_V%mindepth)/PPM_V%ddepth+0.5 )*num_lonperdepth*num_latperlon  &
        + int( (lon-PPM_V%minlon)/PPM_V%dlon+0.5)*num_latperlon &
        + int( (lat-PPM_V%minlat)/PPM_V%dlat+0.5) + 1
```

”

Appendix B

The relocation process of event 2003208:

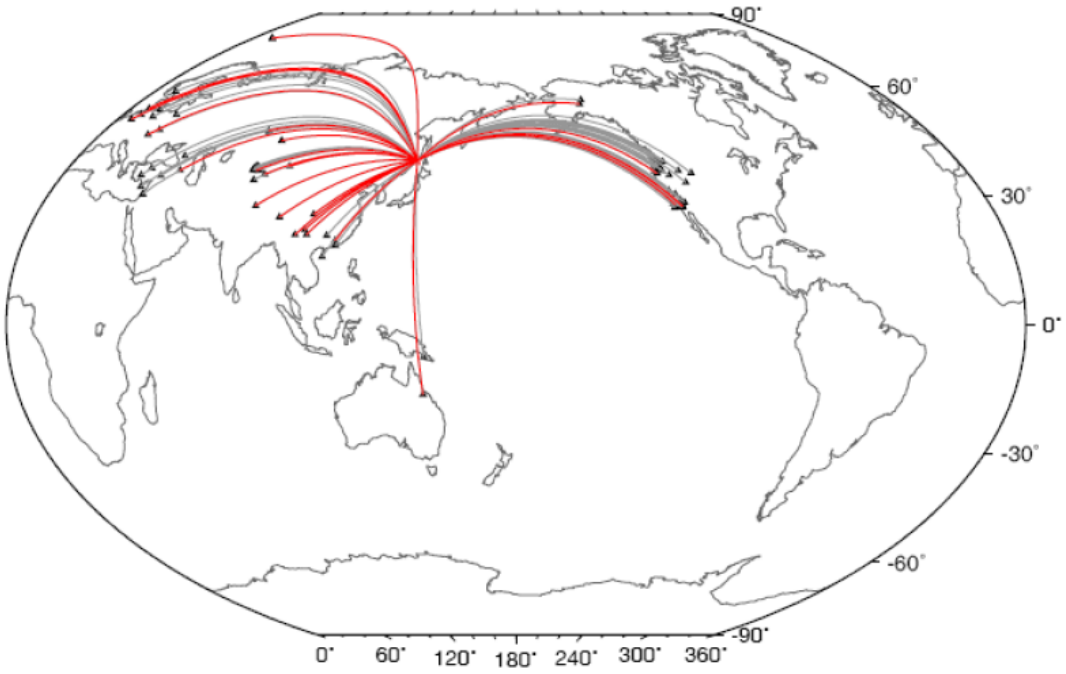

Figure B1: The stations (black trianlges) and raypaths used for relocation of the event 2003208. The raypaths with high SNR (Signal-to-Noise Ratio) of both S and sS are plotted (black lines). Red lines represent selected raypaths (good azimuth coverage) for relocation.

Appendix C

The file designed for inputting the parameters for our modeling:

```
[CitcomS]
steps = 2000              ; number of time steps

[CitcomS.controller]
monitoringFrequency = 20 ; how often outputs are created

[CitcomS.solver]
datafile = cookbook5
datadir_old = ./ic        ; the directory to read the initial (temperature) conditions
datafile_old = cookbook5
rayleigh = 4.07e+08       ; Rayleigh number
verbose = 1

[CitcomS.solver.bc]
topvbc = 1        ; assume the velocity of the top boundary is constant

[CitcomS.solver.param]
file_vbcs = on
start_age = 55
```

```
lith_age=1
lith_age_file=./lith_age/age.dat
lith_age_time=1
lith_age_depth=0.015

vel_bound_file = ./velocity/bvel.dat   ; update the velocity of the top boundary
mat_control=1
mat_file=./mat/mat.dat            ; set the pre-exponent factor of the viscosity

[CitcomS.solver.ic]
tic_method = -1                ; initial conditions are red from datafile
solution_cycles_init = 0

[CitcomS.solver.mesher]
coor = 1
coor_file = ./coor.dat          ; the file sets the coordinates of the grids
nprocx = 1                  ; how many CPUs used for x direction
nprocy = 2
nprocz = 2
nodex = 17                  ; how many nodes/grids in x direction
nodey = 65
nodez = 33
```

```
[CitcomS.solver.tsolver]
finetunedt = 0.75
monitor_max_T = on
[CitcomS.solver.const]
z_lmantle = 0.10516

[CitcomS.solver.phase]
Ra_670 = 0              ; the effect of the 660 is not considered
clapeyron670 = -0.0235
transT670 = 0.70
width670 = 0.0058

[CitcomS.solver.visc]
num_mat = 4             ; how many layers with different viscosity
visc0 = 1,1,1,1
TDEPV = on
viscE = 1,1,1,1
viscT = 1,1,1,1
VMIN = on
visc_min = 0.01
VMAX = on
```

visc_max = 100.0